A Microfluidic Volume Sensor for Single-Cell Growth Measurements

Wenyang Jing

THESIS SUBMITTED IN PARTIAL FULFILLMENT OF THE REQUIRMENTS FOR THE DEGREE OF

MASTER OF SCIENCE

In the Faculty of Graduate Studies (Physics)

uOttawa

L'Université canadienne
Canada's university

Abstract

The multidisciplinary field of microfluidics has shown great promise for research at the interface of biology, chemistry, engineering, and physics. Laminar flow, versatile fabrication, and small length scales have made microfluidics especially well-suited for single-cell characterization. In particular, the evaluation of single-cell growth rates is of fundamental interest for studying the cell cycle and the effects of environmental factors, such as drugs, on cellular growth. This work presents aspects in the development of a microfluidic cell impedance sensor for measuring the volumetric growth rate of single cells and covers its application in the investigation of a new discovery relating to multidrug resistance in *S. cerevisiae*. While there are many avenues for the utilization and interpretation of growth rates, this application focused on the quantitative assessment of biological fitness—an important parameter in population genetics and mathematical biology. Through a combination of growth measurements and optics, this work concludes a novel case of bet-hedging in yeast, as well as the first ever case of bet-hedging in eukaryotic multidrug resistance.

Statement of Originality

The content presented in this document is, to the best of the author's knowledge, the product of original work performed by the author at the University of Ottawa under the supervision of Professor Michel Godin.

Parts of Chapter 2 cover aspects from the following publication:

Riordon J, Nash M, **Jing W**, Godin M. *Quantifying the volume of single cells continuously using a microfluidic pressure-driven trap with media exchange*. Biomicrofluidics. 2014;8(1):011101.

The vast majority of Chapter 3 includes large parts of an, as of yet, unsubmitted manuscript written by the author titled:

Microfluidic Measurements of Single-Cell Fitness Show Bet-Hedging in Eukaryotic Multidrug Resistance
Wenyang Jing, Brendan Camellato, Afnan Azizi, Ian J. Roney, Mads Kaern, and Michel Godin.

In partial fulfillment of the requirements for the degree of Master of Science (Physics) at the University of Ottawa, this work was presented at the Ottawa Carleton Institute for Physics graduate student symposium:

Jing W and Godin M. *Microfluidic Volume Sensing of Single Cells.* Ottawa Carleton Institute for Physics. May 2015.

Statement of Contributions

In the aforementioned publication, the author contributed to the photomask design, the microfabrication, and the testing of devices. Further studies and modifications afterwards were done by the author, including the addition of a sieve valve, further electrical optimization, electrochemical investigations, and changes to fabrication protocols. The last of which also includes contribution from Benjamin Watts. The LabVIEW® code used was predominantly the work of Jason Riordon and Mike Nash, with minor changes made by the author. The experimental setup was assembled by Jason Riordon.

For the study of bet-hedging in yeast multidrug resistance, the GFP-tagged strain used was created by Afnan Azizi. Frozen cell stocks were provided by Afnan Azizi and Hilary Phenix. The discovery of bimodal expression of the PDR5 gene was made by Afnan. For the growth measurements and the evaluation of fitness, the author performed all the culturing, all the experiments, and all the data analysis. The author wrote the introduction, parts of the material and methods, the results, the discussion, and the conclusion. Lastly, all figures in this thesis, unless noted otherwise, were created by the author.

Acknowledgements

I would first like to express my utmost gratitude to Dr. Michel Godin for the opportunity and the guidance he has provided in helping me learn and mature in the area of scientific research. He has set an example to follow. This experience has taught me many skills and has indelibly affected my research interests and future goals. I can safely say that I have emerged more confident and wiser than when I started, and I thank Michel from the bottom of my heart.

I would also like to thank Dr. Jason Riordon, without whom this project would most certainly not exist. He was a good mentor during the months when we worked together and continued to offer guidance even after his departure.

I am also very grateful to Dr. Benjamin Watts, whose expertise and friendliness proved invaluable in my learning of microfabrication and in facing the slew of technical problems that hampered progress. He became someone whom I could easily go to in the lab on a daily basis to discuss issues with and bounce ideas off of. I thank him deeply for his mentorship.

My project also relied on collaborating with Dr. Mads Kaern's group here at uOttawa. I'd like to thank him and his group for introducing me to how the tried and true organism that is yeast still has much more knowledge to offer us. I would especially like to thank Afnan Azizi for the enjoyable talks we had and for the invaluable work he has done in bringing this project to life and making our paper a reality. I am also very grateful to Hilary Phenix and Ian Rooney for their willingness to answer my questions and their advice on yeast culturing. Hilary's longstanding guidance and generosity, in particular, have helped to keep things going.

I would also like to thank Daniel Modulevsky, Sebastian Hadjiantoniou, and Dr. Tina Hasse for their advice with imaging. Their efforts have increased my understanding of microscopy and I have very much liked hearing about their work as well.

My gratitude also goes out to others I have had the pleasure of sharing the lab with: Ainara Benavente, Ali Najafi Sohi, Cedric Eveleigh, Eric Beamish, Keith Dennis Ludlow, Nicolas Monette-Catafard, Radin Tahlvidari, Sophie Chagnon-Lassard, and Veronika Cencen. They have all taught me new things and made for a friendly environment both inside and outside the lab.

Lastly, I would like to thank my loving parents for their continued support in my life and my decisions. Without them, I probably would have not found my way to uOttawa.

Table of Contents

Legend

- AC – Alternating Current
- DC – Direct Current
- DI-H_2O – Deionized Water
- GFP – Green Fluorescent Protein
- HE – High Expressing
- LE – Low Expressing
- MDR – Multidrug Resistance
- NaCl – Sodium Chloride
- PDMS – Polydimethylsiloxane
- PDR – Pleiotropic Drug Resistance (such as the PDR5 gene)
- *S. cerevisiae* – *Saccharomyces cerevisiae* (budding yeast or brewer's yeast)

List of Figures

List of Tables

1. Introduction

1.1 Microfluidics: Its Foundations and Applications

Microfluidics is the science and technology of small fluidic systems, where small implies nanoliter to femtoliter volumes and linear dimensions ranging from a few microns (μm) up to hundreds of microns. These length scales create a unique regime of fluid flow that is not seen on the macroscopic scale where convection dominates. Instead, viscous forces are greater than inertial forces and mixing does not readily occur. In addition to the fluid physics, the small length scales also imply small components. Tiny channels, electrodes, pumps, and valves are engineered into devices that can fit into the palm of an adult human hand—no bigger than a standard microscope slide and often smaller. These devices have been exploited for chemical reactions[1], integration with optics[2], single-molecule detection[3], and the precise manipulation of cells[4]. All of this has led to the moniker: *lab-on-a-chip*, a term that expresses the ideal of miniaturization, for cheaper and more efficient processes. Naturally, the benefits to chemistry and the life sciences are immense. But for the area of public health in particular, microfluidics promises the development of point-of-care (POC) diagnostics, as epitomized by the classic blood glucose meter. Such technologies could revolutionize the accessibility of biomedical tests to the global community[5]. Microfluidics is therefore a field that both derives from and impacts multiple disciplines.

The first advantage in microfluidics comes from fluid physics[6], which is generally described by the Navier-Stokes equation and the continuity equation[7], respectively:

$$\frac{\partial \boldsymbol{u}}{\partial t} + (\boldsymbol{u} \cdot \nabla)\boldsymbol{u} = -\frac{\nabla P}{\rho} + \nu \nabla^2 \boldsymbol{u} + \boldsymbol{g} \quad (1)$$

$$\frac{\partial \rho}{\partial t} + \nabla \cdot (\rho \boldsymbol{u}) = 0 \quad (2)$$

Here $\boldsymbol{u}$ is the velocity vector field of the fluid, P is the pressure, ρ is the fluid density, ν is the kinematic viscosity of the fluid, and $\boldsymbol{g}$ is the acceleration vector field due to external forces, such as gravity. The two terms of interest in the Navier-Stokes equation are the inertial

term: $(\boldsymbol{u} \cdot \nabla)\boldsymbol{u}$, and the viscous term: $\nu\nabla^2\boldsymbol{u}$. At the macroscopic level, the inertial term is dominant and gives rise to convection and turbulence, both of which greatly promote the transport of molecules through the fluid as well as mixing. But in microfluidics, the opposite is true. The condition $\nu\nabla^2\boldsymbol{u}$ >> $(\boldsymbol{u} \cdot \nabla)\boldsymbol{u}$ can be met through either having a highly viscous fluid, like honey, or very small length scales, like those in microfluidics. The dimensionless parameter that describes the relative magnitude of these two terms is known as the Reynolds number (Re), and is the ratio of inertial forces to viscous forces[7]:

$$Re = \frac{U^2/L}{\nu U/L^2} = \frac{UL}{\nu} \quad (3)$$

Here *U* is the characteristic flow speed and *L* is the characteristic length. The Reynolds number essentially compares the momentum (energy being carried) to the friction (energy dissipation) in the system. At high Reynolds numbers, where inertial forces are much larger, turbulence occurs. Indeed, the inherent nonlinearity of the Navier-Stokes equation as well as its analytical intractability comes primarily from the second power of the velocity in the inertial term. The transition to persisting turbulence typically begins at a Reynolds number of ~2000, but in microfluidics, the Reynolds number is typically less than 1. For the device presented in this work, *Re* is estimated to be ~0.006. Thus by arguing that the inertial effects are small and can be neglected, the Navier-Stokes equation can then be linearized to:

$$\frac{\partial \boldsymbol{u}}{\partial t} = -\frac{\nabla P}{\rho} + \nu\nabla^2\boldsymbol{u} + \boldsymbol{g} \quad (4)$$

This result closely resembles the heat or diffusion equation, where the kinematic viscosity plays the role of the diffusion coefficient. Flow in this regime is therefore marked by the diffusion of momentum rather than the convection of momentum, as is the case on the macroscopic scale. In fact, diffusion is the process that must be relied upon for mixing as turbulence and convection have become negligible. But this is made up for with predictability. Flow at low Re is purely laminar, where each lamina or layer of fluid slides past one another without convective mixing. The velocity profile, depicted with red arrows in Figure 1.1, is smooth and orderly in laminar flow. These red arrows are called streamlines, and represent the paths that particles would travel in the fluid. Therefore in laminar flow, it is easy to predict where objects will go if

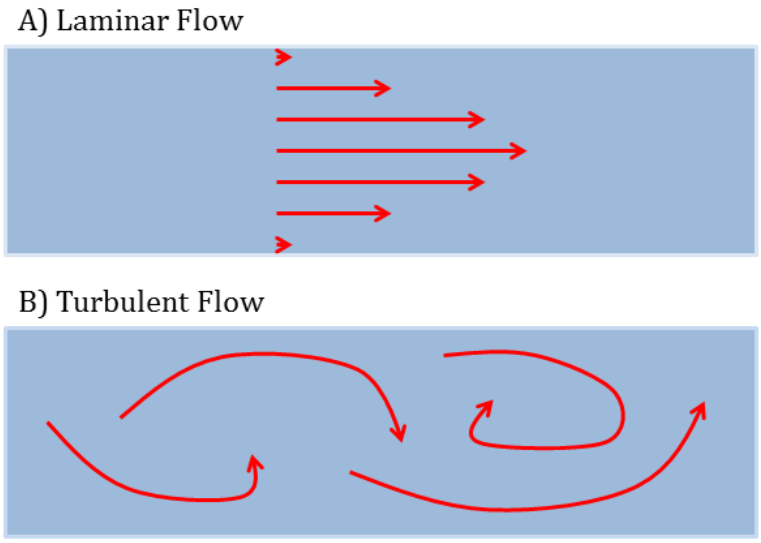

Figure 1.1 The red arrows illustrate streamlines, which depict the trajectories of fluid flow. They also represent the velocity profile of the flow in a channel or pipe. A) Laminar flow is characterized by organized streamlines. B) Turbulence is characterized by chaotic flows with unpredictable streamlines as time goes on.

the paths of the streamlines are known—not difficult to simulate for all kinds of channel layouts by using computational software such as COMSOL®. In addition, the liquids used in microfluidics are incompressible (constant density in space and time), which simplifies equation (2) and leads to the conservation of volume, allowing for the volumetric flow rate to be treated as an analog of electrical current. The conditions of incompressibility and laminar flow consequently make Poiseuille's law[8] and the Segré-Silberberg effect[9] applicable. Hence, these factors permit the dependable and predictable control of the pressures and of the hydrodynamics, forming a cornerstone of microfluidics.

To make use of the small-scale fluid physics however, proper sized channels must be engineered. It is here that the microfabrication methods of the silicon microelectronics industry serve as a pillar for microfluidics[10]. The ways of photolithography, dry etching, and wet etching have allowed for the microfabrication of fluidic channels in silicon and glass[11], as well as for the patterning of thin film metals[12]—to make on-chip electrodes with, for example. The short wavelengths of the UV radiation in photolithography and the creative potential of photomask design also mean that both very small and very diverse geometries can be fabricated. While these techniques are powerful and tried for semiconductors, making use of

only rigid substrates such as silicon or glass has its drawbacks. For example, their hardness prevents the implementation of pumps and valves, their chemical structures do not offer the gas permeability needed for certain biological applications, and in the case of silicon, a lack of transparency is problematic for microscopy or integration with optics. But these issues have been solved with the invention of soft lithography[13], a technique that replicates structures using elastomeric casts, molds, and stamps. It stands as a potent complement to photolithography. Through the latter, silicon wafers patterned with various features made from photoresist can serve as master molds. Then using soft lithography, liquid elastomers can be cast on the molds and then cured to make flexible structures that have transparency, gas permeability, and can still be bonded to a hard substrate like glass. The advent of this method has led to the fabrication of multilayered devices with pumps and valves[14], and even to the replication of some of the functions in electronic integrated circuits using an elastomeric microfluidic chip[15]. And so as a result of their low costs, precision, quick prototyping, and reproducibility, these techniques have precipitated a huge rise in the use of microfluidics over the past decade, especially for life science research[16].

The ability to fabricate microfluidic devices with complex functions and small structures includes the appeal of requiring very small volumes of samples and reagents when putting the devices to use. For the purposes of chemical detection, this is of course a huge boon, and was in fact one of the earliest motivations to develop microfluidics[17]. Another outcome that has been made possible is the unique generation and manipulation of tiny droplets. Droplet microfluidics has recently gained significant traction due to its ability to individually encapsulate cells and reagents[18], thus offering many benefits to biology and chemistry. It has even helped initiate the subfield of digital microfluidics[19]. The use of small volumes, however, has been pushed still further with the microfluidic integration of solid-state nanopores[20], which are capable of sensing short strands of DNA. But in order to also exploit the small volumes for chemical reactions, substances must be able to effectively mix, and therefore a conflict arises. Despite the advantages of laminar flow, diffusion-mediated mixing alone is simply not sufficient. Yet the ways which microfluidic devices can be fabricated once again help to advance the field further through the engineering of more complex components and configurations that

enable both active and passive modes of mixing[21]. The active mixing can come from acoustic[22], electric[23][24], or magnetic forces[25], made possible by the integration of thin film metal electrodes, magnets, or piezoelectric motors and substrates. The passive mixing derives from making clever use of the versatile lithographic processes and creating channel geometries and structures that manipulate the hydrodynamics to promote advection. The results could be enhanced diffusion[26] or even the induction of localized turbulence[27]. But the beauty of all the aforementioned methods is that they can be combined and multiplexed in different ways to create custom microfluidic chips; a device that encapsulates cells in droplets, for example, could integrate electrodes and selectively manipulate those droplets using the electric forces of dielectrophoresis (DEP)[24]. With such flexibility in hand, it should be no surprise that powerful tools like those stated above have also been applied to the sorting and characterization of cells.

The appropriate length scales, the control provided by valves, and the applicability of acoustic, electromagnetic, hydrodynamic, and even optical forces make microfluidics well-suited for single-cell applications. A prominent one is the separation and sorting of cells[28]. The standard has been fluorescence-activated cell sorting (FACS), where optical differentiation of cells tagged with fluorescent labels are encapsulated in charged droplets and sorted electrostatically. This requires charged droplets, is expensive, and can be difficult to use. Consequently, efforts have been made in microfluidics to perform sorting both with and without labels. Distinctive methods include: the use of acoustic radiation pressures[29] and surface acoustic waves (SAW)[30] to sort by size, the dielectrophoretic sorting of labeled cells[31] and of unlabeled cells by their dielectric properties[32], the magnetic detection and separation of magnetically labeled cells[33], the employment of electromagnetic radiation pressures from focused laser beams[34], and the use of hydrodynamic forces[35], such as inertial lift[36]. These technologies enable the detection and purification of specific cells of interest with the additional benefits of low sample volumes, thus they hold great potential for the development of point-of-care diagnostics. Sorting, however, is not the only edge that microfluidics has when it comes to cells, for the primary motivation of the work in this thesis has its roots in single-cell characterization.

While the methods for single-cell biochemical characterization are well-established and have taken full advantage of microfluidics[37], they often require markers[38], and are invasive if not outright lethal to cells[39], since lysis is usually required. Single-cell biophysical characterization on the other hand tends to be nonlethal and is label-free. The typical properties assessed fall under two categories: mechanical and electrical[40]. These include the cell's dielectric traits, density, mass, size, and stiffness. The characteristic that has arguably received the most attention from biology and medicine is stiffness, as changes in cell deformability are known to occur during stem cell differentiation[41] and to be major indicators of disease[42]. For example, when compared to normal cells, leukocytes from patients with sepsis are less deformable[43], erythrocytes of various blood disorders are stiffer[44], and cancer cells have been shown to actually be more elastic[45]. Cell deformations can be measured with constriction channels, which emulate the environment of capillaries and are easily constructed with the microfabrication techniques of microfluidics. They have been used to characterize the stiffness of blood cells[46] and cancer cells[47] via the image analysis of entry times, transit times, and transit velocities through these constriction channels. The fluid physics at these length scales has also been exploited in the hydrodynamic stretching of red blood cells[48] as well as leukocytes and cancer cells[49]. Other methods of inducing cell deformations include the use of electrical and optical forces[40], made possible by the integrative versatility of microfluidic chips. For cell mass and density, a small class of suspended microchannel resonators (SMR) has been developed[50][51]. They can precisely measure the buoyant mass of cells by detecting changes in the resonant frequency of a hollowed out microcantilever as a cell flows through it. But of all the physical properties, size is perhaps the most widely evaluated[52][53], and is intimately tied to the dielectric characterization of cells. Because while the fundamental attributes of conductivity and permittivity can be measured with dielectrophoresis and electrorotation[54], it is the impedance measurement of cells that is used more often[55]. Not only is the impedance measurement able to reveal information about the capacitive and ohmic contributions from different parts of cell, it is the way by which cell size is most often characterized. In fact, this method of quantifying size forms the basis of the volume sensor presented in this work.

1.2 Impedance Cytometry

Cell impedance sensing is inherently label-free and has its origins in the Coulter principle[56], patented by Wallace H. Coulter in 1953. The concept is as follows: when a particle passes through an orifice or sensing volume which has ionic current flowing through it, a drop in the current will occur because the impedance of the detection volume has increased due to the displacement of ions and the occupation of that space by the particle. This current drop is known as an impedance pulse, the magnitude of which is directly proportional to the volume of the particle that generated it. A typical current trace is illustrated in Figure 1.2. Coulter counters, which have been commercially available for a long time, operate on this principle to quickly count and size particles, most commonly blood cells. With this direct measurement of volume and a cubic sensitivity to the radius, Coulter counters are significantly better for particle sizing than optical flow cytometers[57]. Optical methods, in general, must contend with varying refractive indices, suboptimal resolutions, bulky optics, and the poorer process of trying to extract size from light scattering or 2D images based upon the strict assumption that a cell is spherical. Therefore, a miniaturization of the Coulter counter would become a powerful hand-held tool for biology and medicine.

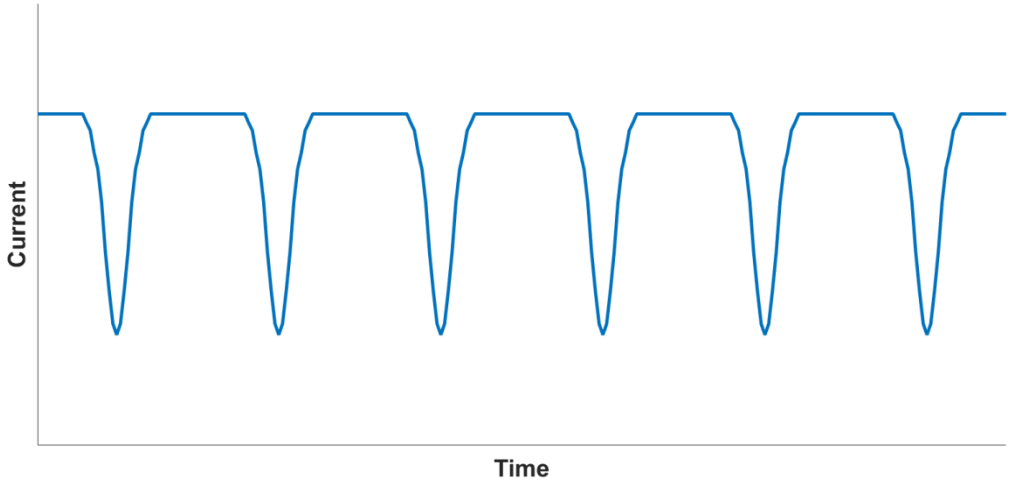

Figure 1.2 An idealized current trace of transient impedance pulses, where each drop corresponds to a passing cell or particle. The amplitude of the drop is correlated to volume through the Coulter Principle.

Conventional Coulter counters use silver/silver chloride (Ag/AgCl) electrodes with a DC potential as both are easy to implement and DC avoids the frequency response of cells to an AC

signal[58]—to be elaborated on later. This kind of setup for measuring cell impedance was integrated into microfluidic devices that used both mechanical deformability and impedance characterizations to biophysically assess red blood cells[59] and to classify different cell types[60]. But for the broader purposes of microfluidics and lab-on-a-chip devices, the use of non-polarizable electrodes, such as Ag/AgCl ones, has some key drawbacks. First: they must be inserted and so are less compact, second: they are depleted over time, and third: their geometries cannot be easily manipulated in many ways. Fortunately, the microfabrication techniques for thin film deposition can be employed to create fully integrated on-chip electrodes formed from thin film metals. These electrodes can be patterned diversely through photolithography and have also been used as an important source of electric fields for some of the other previously stated applications, such as dielectrophoresis. In microfluidic chips, the primary substrate for deposition is typically glass. On top of the glass is deposited a very thin adhesion layer, such as chromium or titanium, followed by the main electrode layer, which is usually a noble metal like gold or platinum. These types of thin metal electrodes are polarizable, which means they do not rely on electrochemical reactions to generate ionic current, as is the case for non-polarizable electrodes. In fact, the first reported microfluidic Coulter counter[61] used microfabricated platinum electrodes. But a main feature in this particular Coulter counter was that an AC signal was applied instead of a DC one. This is because while DC potentials are appropriate for driving the electrochemical cell in non-polarizable electrodes, the preferred thin metal electrodes for microfluidic chips face some problems with a DC potential. Depending on the voltage, DC can cause hydrolysis and generate gas bubbles that interfere with the measurement and lower the lifespan of the device[62]. But the foremost issue is that it contributes to the buildup of the electric double layer (EDL)[63] at the electrode-liquid interface. This double layer behaves like a capacitor, and therefore has impedance. The complex impedance of a capacitor, Z, is given by:

$$Z_{capacitor} = \frac{1}{j\omega C} \quad (5)$$

where j is the imaginary number, ω is the applied angular frequency, and C is the capacitance. Given that the capacitive impedance is inversely proportional to the driving frequency, a DC

signal would cause a significant attenuation of the applied potential[64]. This of course poses a large problem when trying to measure the impedance of a cell or the solution, as the EDL impedance will dominate the measurement. Thus an AC signal that charges and discharges the electric double layer at the electrode surface will help to mitigate this so-called electrode polarization impedance[65], especially at higher frequencies.

Even with an AC signal, the Coulter counter technically still functions at only one frequency, and so is limited to just counting and sizing particles. However, it is the application of AC signals that makes further electrical characterization possible, as the frequency needs-not be fixed and can be swept; this technique is known as impedance spectroscopy[66]. When using a pair of electrodes to measure the impedance of a cell occupying the detection volume, the contributions to this impedance come from the electric double layer, the ionic solution, and the cell itself, as shown in Figure 1.3. The simplest model of a cell, however, consists of a single resistor and capacitor in series with each other, representing the cytoplasm and plasma

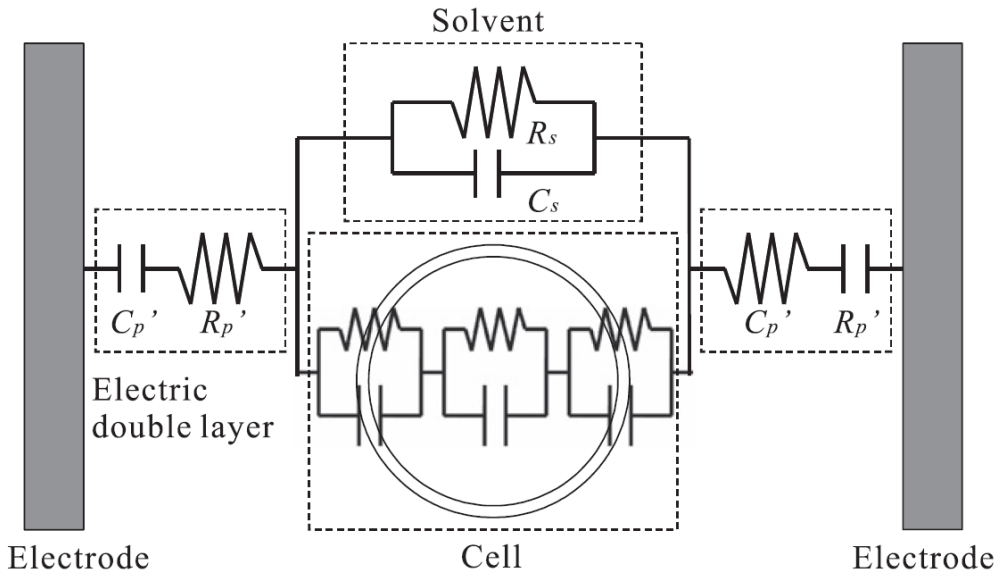

Figure 1.3 Each part of the detection volume: the electric double layer, the solution, and the cell, are modeled with constituent capacitors and resistors. *Cp'* and *Rp'* represent the respective capacitance and resistance of the electric double layer at the electrode surface. The bulk electrolyte solution has its own capacitance and resistance, *Cs* and *Rs*, respectively. The cell itself has two components: the plasma membrane and the cytoplasm. Each is modeled as a resistor and a capacitor in parallel with each other. While the parameters for the solution and EDL are highly dependent on the salt, the concentration, and the type of buffer used, the cell's cytoplasm has a typical conductivity of 0.5 S/m and the membrane has a typical capacitance per unit area of 1 μF/cm^2. (Reproduced with permission from the authors[64])

membrane respectively. But based on the circuit diagram in Figure 1.3 and equation (5), it is clear that the dielectric response of cells will vary with frequency, therefore determining which circuit element will be the leading contribution to the overall impedance. This frequency-dependent effect is known as dielectric dispersion[67], for which there are three regimes in cells: α-dispersion, β-dispersion, and γ-dispersion[68]. α-dispersion occurs at low frequencies (a few HZ to a few kHz), where it is believed that the ionic diffusion in the electric double layer surrounding the cell is the prevailing component of cellular impedance. This is difficult to measure, however, because the electrode polarization impedance dominates all others at these frequencies. β-dispersion occurs between 1 to 100 MHz. Here, the prevailing component of cellular impedance comes from the charge buildup across the plasma membrane due to different charge carrier relaxation times; this is known as Maxwell-Wagner polarization[69]. In the frequency range between these two dispersions, the insulating behavior of the plasma membrane is most apparent. A particular study[61] showed that in a region below 1 MHz, the impedance value is strongly correlated to the cell size or volume, and so is sensitive to cell morphology and is ideal for Coulter counters. In addition, the electrode polarization impedance (Pt-black electrodes) was shown to be completely negligible at 100 kHz and above. But beginning at 1 MHz, the impedance became more reflective of the plasma membrane capacitance rather than the cell size, consistent with the phenomenon of β-dispersion and also useful for the characterization of the cell membrane. The last regime of γ-dispersion occurs at microwave frequencies and is due to the polarization of water molecules. In this high frequency domain, the plasma membrane acts as a short and the cell behaves as a resistor, thus allowing the electrical properties of the cytoplasm to be probed. Therefore, by sweeping the various frequency ranges with impedance spectroscopy, information about different parts of the cell can be obtained. These applications of impedance for counting, sizing, and measuring the various dielectric responses of cells are collectively known as impedance cytometry[55]. Such methods have been utilized in numerous studies, some of which include: the label-free isolation of CTCs[70], the electrical characterization of cell deformability[64], the quality assurance of nanomedicines[71], and even the assessment of anti-cancer drug efficacy[72]. In the work

presented here, the Coulter principle is applied for the quantification of single-cell growth rates in order to evaluate biological fitness.

1.3 Cell Growth and Biological Fitness

Cell growth is physically the increase of mass and size as a cell synthesizes nucleic acids and proteins for division. This fundamental process governs reproductive rates and population level dynamics, thus underlying the very perpetuation of life itself. However, cells can grow differently depending on where they are in the cell cycle[73]. In the more simplistic prokaryotes, the cell cycle consists of three phases known as the B, C, and D periods[74]; they constitute the steps of binary fission, the mechanism for prokaryotic reproduction.

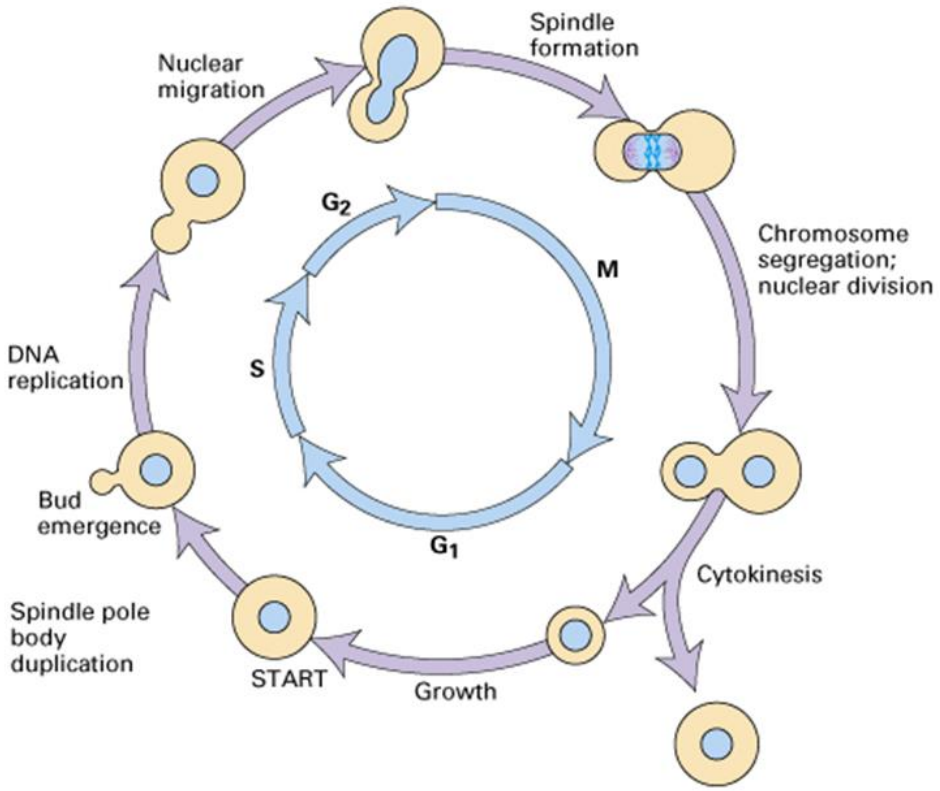

Figure 1.4 This is an example of the eukaryotic cell cycle with budding yeast. Each phase of the cell cycle is characterized by different growth rates. The G1 phase is where the cell grows and prepares for DNA synthesis. The G1 checkpoint (not shown) must be passed to proceed into S phase, where DNA replication occurs. In G2, the cell resumes growth and does so particularly quickly. Successful procession through the G2 checkpoint (not shown) leads to M phase, where mitosis occurs. Finally, the cell completes its division through cytokinesis (© G.H. Zheng 2005).

But it is the more complex eukaryotic cell cycle that is of particular interest, not just because it concerns the study of higher organisms like us, but also because eukaryotes are generally more difficult to study than the fast-growing prokaryotes, and therefore makes microfluidics especially useful. Much of what is known about eukaryotes comes from observing the model organism that is yeast[75]. Shown in Figure 1.5 is the eukaryotic cell cycle, as exemplified by budding yeast (*S. cerevisiae*). Common to both prokaryotes and eukaryotes, however, are cell cycle checkpoints[76][77]. They exist to ensure that a cell is fit and prepared for the transition to the next phase in the cycle. Disruptions to these vital checkpoints can result in growth abnormalities, DNA replication errors, and even death[78]. In fact, mutations that alter the regulation by checkpoints and other pathways in the cell cycle are known to cause cancer[79]. This knowledge has been exploited to improve chemotherapy[80], and therefore a better understanding of the complexities in the cell cycle could profoundly impact both biology and medicine. In this regard, cell growth can be used to help study the phases and checkpoints of the cell cycle. For example, it was suggested that measurements of individual cell growth were necessary in order to resolve a disagreement about whether cell size checkpoints played a role in the mammalian maintenance of size homeostasis[81]. Then, a later study, which used a suspended microchannel resonator to evaluate the mass growth rate of single cells, found that there was a critical growth rate instead of a critical size that regulated the G1-S transition in mammalian cells[82]. So while the exact mass and size are important physical parameters of growth, the rates themselves can serve as independent factors. But despite the links that connect the cell cycle to cell growth, the coupling between the two is still not well understood[83]. Nonetheless, research has continued to establish correlations between them. One study showed that bacterial cells with slower growth rates employed a different chromosomal replication process compared to cells with faster growth rates[74]. Another study with yeast demonstrated that growth rates are directly related to gene expression, metabolic activity, stress response, and the number of cells in the G1 phase[84]. Growth rates in yeast were even shown to be an indicator of cell lifespan and the state of senescence[85]. But in light of the accumulating experimental data, a solid theoretical framework to help organize the many observations is still lacking. Recent efforts include the mathematical modeling of bacterial

cell size regulation[86], of the coordination of cell growth and cell division[87], of the interdependence of cell growth and gene expression[88], and of the relationship between bacterial growth laws and the evolution of energy efficiency[89]. These studies have shown that the current theoretical understanding is only beginning to make sense of the existing knowledge, and that further data and validations are required.

Conventionally, cell growth is measured using optical density or even cell counting, both of which produce population level averages and lack the precision that single-cell growth rate measurements can provide. Thus microfluidic technologies would not only be able to offer better and more precise data, they would also be able to investigate cell growth in new and innovative ways under the highly controlled conditions provided by microfluidics. The micro-Coulter counter, in particular, also has the ability to sense cell morphology, which is useful, since cell shape is another factor known to regulate cell growth[90], and the mechanisms behind how cells actually regulate their shapes with such high precision is still not well understood[91]. In this work, however, the volume sensor was used to measure single-cell growth rates in order to evaluate biological fitness.

Fitness is a central theme in evolutionary biology and is a measure of the reproductive success of an individual or of a population[92]. It can be mathematically defined in a variety of ways[93] and is conventionally denoted as w. For a continuously growing population, it can be written as[94]:

$$(6)\ \ w = \frac{N(t)}{N_0}$$

where $N(t)$ denotes the number of individuals at some time t, and N_0 represents the number of individuals initially. This definition is usually termed absolute fitness, as it compares individuals from the same population possessing the same genotype or phenotype. When comparing distinct populations, relative fitness is used instead[94]:

$$(7)\ \ w_r = \frac{N_1(t)}{N_2(t)}$$

Here N_1 and N_2 are the numbers of individuals from each respective group. While there are still many more ways to mathematically analyze and characterize fitness, the basics of this parameter serve as the foundations for theorizing the paths of adaptation on all levels, ranging from genes to populations. However, the theoretical models at present rely on many assumptions and predictions, both of which greatly require further testing and refinement[93]. Since fitness is often evaluated through growth rates[94], the ability to measure this for single cells in place of population level averages would bring a finer degree of precision to the experimental efforts that are needed. Microfluidics is capable of this and also boasts superb control of the cell environment. In addition, the easy integration with microscopy means that all the standard optical methods of assessing cells—such as with dyes, GFP, and other labels—become available as well. But the environmental control, in particular, allows for the study of the vital role that the environment plays in shaping evolution. In fact, a recent study showed that sensitivity to environmental noise is a major factor in the determination of fitness functions[95]. Microfluidics has already begun to contribute to this with the publication of a device[96] that was able to measure competitive fitness through image-based sizing and in a dynamically changing environment. Yet, these advantages can impact more than just evolutionary biology, for the rise of systems biology[97] means that microfluidics can be applied to both perturb cellular pathways and to assess the systemic response resulting from such perturbations. The work described in Chapter 3 contributes to these areas of active research through the investigation of a new discovery concerning phenotypic heterogeneity in the expression of a gene in *S. cerevisiae* that grants multidrug resistance. We hypothesized this to be a case of bet-hedging, and in order to confirm this, we used the microfluidic volume sensor presented in Chapter 2 to quantify the fitness of each phenotype by measuring the volumetric growth rate of cells in different on-chip environments. By establishing that each phenotype granted an environment-dependent fitness advantage, these results concluded the first known case of bet-hedging in eukaryotic multidrug resistance.

2. Materials, Methods, and Device Characterization

2.1 Device Design and Proof-of-Concept

This project began with the testing and design of a microfluidic volume sensor that applied the Coulter Principle with the use of microfabricated on-chip electrodes.

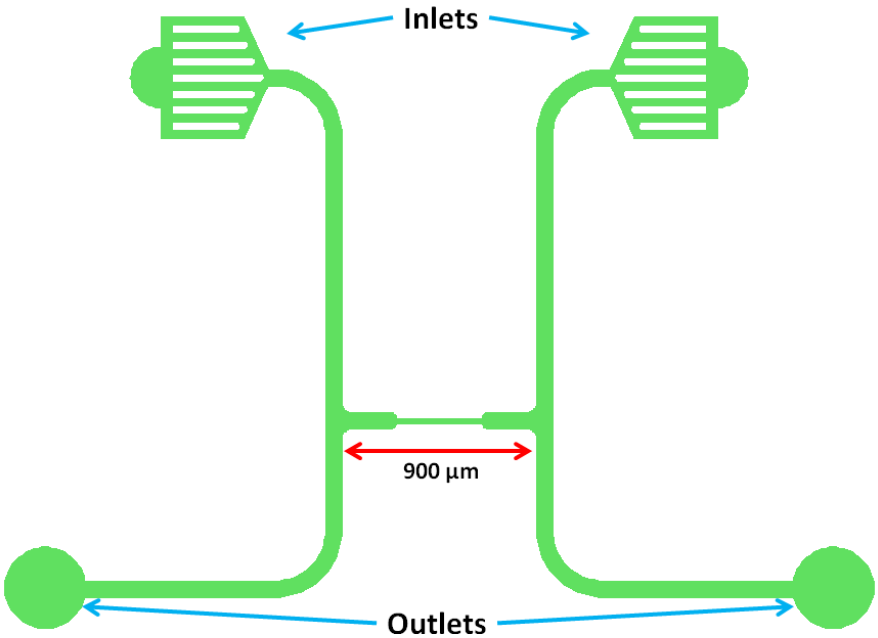

Figure 2.1 The photomask design for the channel layer of the volume sensor device. The central channel of the H-shape (from prior work) is the sensing channel, where the cell would be cycled over the electrodes. The inlets include long posts that form corridors for the fluid. This divides the flow rate so that particles do not accelerate so suddenly when entering the main (bypass) channels that form the sides of the H. These corridors also serve the purpose of stopping large debris from clogging the device.

The goal was to build a device that could trap a single cell and then quantify its growth over time by constantly shuffling it back-and-forth across the electrodes, making a volume measurement each time. Initial channel designs that were tested used wider H-channels than what is shown in Figure 2.1 and some even incorporated serpentine geometries into the sensing channel. Consequently, these types of designs all had a much longer sensing channel, so the distance from the bypass channels to the center—where the electrodes were located—was greater. These configurations produced a problematic sinusoidal oscillation of the baseline current when the cell was cycled back-and-forth across the electrodes. The slopes from the oscillating baseline made computing the depth of the impedance pulse less accurate, and could

even worsen to the point where the LabVIEW® program would recognize a valley of the sinusoidal oscillation as an actual event. A curiosity, however, was that it seemed to be worse with the yeast media than with the simpler solution of DI-H_2O and NaCl. While the reasons for all of this were never understood, the design of the much narrower H-channel, as shown in Figure 2.1, seemed to solve the problem. The central sensing channel in the design has a total length of 900 μm from the left bypass channel to the right, but its thinner portion is 420 μm long and 25 μm wide. Still, some mild oscillations were observed to occur at times, though not very often. They appeared to have been correlated with either anomalous behavior from the pressure regulators or debris buildup within the flow paths. For the latter, baseline oscillations were found to be greatly reduced or eliminated after concerted cleaning efforts. A key change following the cleaning was that the pressure differentials established by the two outlet regulators were smaller and steadier during experiments when the fluid flow in the sensing channel was being continuously reversed. And so in conjunction with the pressure regulator anomalies, the observed oscillations were most likely due to pressure effects—at least for the design in Figure 2.1. This makes sense in the context of streaming current[98]—the flow of electrolytes driven by a pressure gradient—as different flow speeds from each direction caused by very unequal pressure differentials would result in two distinct levels of measured ionic current depending on which side the fluid was coming from. This could produce an oscillation-like effect in the baseline as the fluid flow is periodically reversed. But another reason that the design in Figure 2.1 was settled upon was the concern over the diffusion time for nutrients had the sensing channel been too long and the cell remained too far away from the bypass channels. The narrower design thus helped to address this issue as well.

A drawback to having a shorter sensing channel, however, was that there wasn't much room for error and variability during flow reversals. If a cell traveled too far in either direction, it would be pulled into the bypass channels and the trap would be lost. This necessitated the use of sieve valves, which not only made trapping easier—as they could seal off the sensing channel—but were also able to be partially lifted during the experiment to allow fluid flow while still preventing the cell from escaping. In addition, the valves made media exchange on-chip possible through its sealing capability, thereby enabling the introduction of foreign

agents—such as drugs—into the device after a cell had already been trapped. This could even have been done mid-experiment, for example. Together with the microfabricated electrodes, the volume sensor consisted of three layers: the glass the electrodes were patterned on, the channel layer, and the valve layer (fabrication overview in section 2.2). The proof-of-concept for this device was performed using cells from a diploid strain of *S. cerevisiae*, and published in *Biomicrofluidics*[99]. Figure 2.2 is a reproduction of Figure 1A from the publication. This microfluidic volume sensor was also integrated with a microscope (it is upside-down on the microscope stage), which enabled the image shown in Figure 2.2 to be taken. The benefit of this integration was that in addition to the quantitative volume measurements, the cell could also

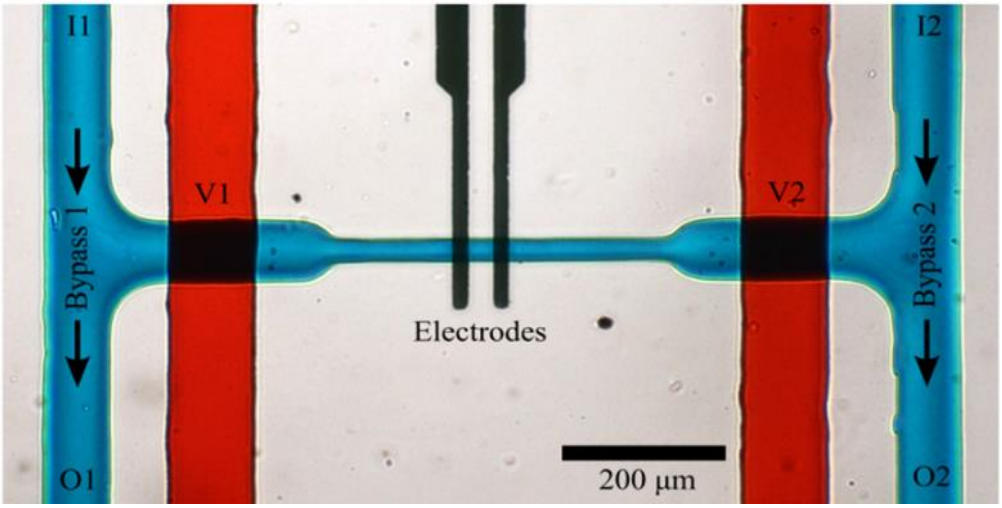

Figure 2.2 The valves, in red, would be sealed when a single cell moved into the sensing channel from either of the bypass channels. The media could then be switched if desired. Each time the cell flowed past the electrodes, an impedance pulse was registered, which then triggered the trapping program to reverse the flow direction through two computer-controlled pressure regulators that were each connected to one of the outlets (O1 and O2). The thin portion of the sensing channel is 20 µm tall and 25 µm wide. The device itself sits upside-down, and bright field images are taken in transmission mode.

be tracked with time-lapse imaging and could be distinguished using optical markers if necessary. In the context of yeast, the imaging is particularly useful for discerning when budding events take place and for estimating the length of time between divisions. The volume itself was determined from a raw measurement of ΔI/I—the change in current divided by the baseline current—using a calibration done with polystyrene microspheres (section 2.4). Shown in Figure 2.3 is a reproduction of Figure 2 from the publication. In addition to demonstrating the

growth measurement and media-exchange capabilities, it was concluded for budding yeast that the volumetric changes over the period of one cell cycle followed a sigmoidal shape—as defined within the measurement precision. While it has already been shown that mass increases exponentially[50], a different growth law between mass and volume is not unreasonable; a study proved that the cell density in *S. cerevisiae* varies over the cell cycle and is cyclical[100], unlike the constant densities of the widely used *E. coli* cells, Chinese hamster cells, and murine cells.

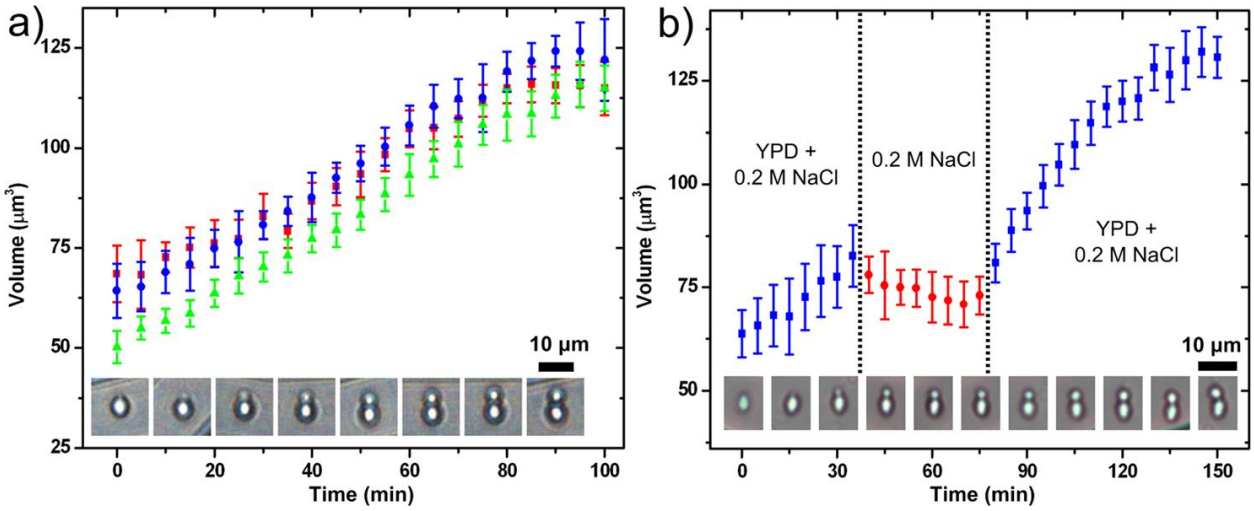

Figure 2.3 Each data point is the average of ~5 min of raw data. The error bars represent the standard deviations of the data that was averaged. A) The growth curves are for three different cells. They were grown in a standard yeast media (YPD) with added NaCl. The salt was required for the ionic displacement needed in a volume measurement. B) This graph demonstrated the device's ability to switch the inflowing media, and therefore the cell's environment. About half-an-hour into the experiment, growth was stopped due to the removal of the yeast media, but it was resumed after switching back.

It should be noted that the magnitude of the electric field is the same for both the work presented in Chapter 3 and for the aforementioned publication, and its average can be approximated to be ~7.07 x 10^3 V/m (with V_{RMS} = 212 mV and the separation between the inner edges of the electrodes being 30 μm). While electric fields can certainly be a cause of stress for cells, it has been shown for this setup that the potential difference induced across the cells is inconsequential[101]. In addition, Figure 2.3 demonstrates that this electric field strength is not a cause for concern as the doubling times are ~2 hours and match with what is expected from regular incubated growth.

Following this publication, the device was augmented with an additional sieve valve over the electrodes based on a study showing that the sensitivity of a Coulter counter could be tuned by changing the channel height using the valve[102]. This centers on the fact that the

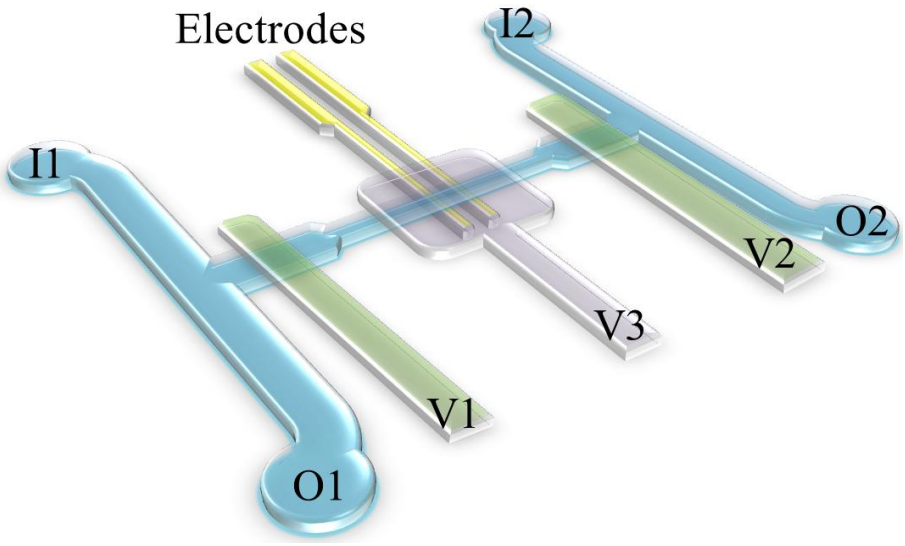

Figure 2.4 This diagram shows a 3D rendition of each layer in the device. During an experiment, a cell moves back-and-forth over the electrodes and predominantly cycles from the left edge of the sieve valve V3 (in violet) to the right edge. I1 and I2 denote inlets 1 and 2, where the sample is flowed in. The tubing for both inlets come from the same vial and so are pressurized equally. O1 and O2 denote outlets 1 and 2. The tubing for each empties into their own vials and are each pressurized independently. Sieve valves V1 and V2 (in green) as well as V3 (in purple) are filled with water. By applying pressure, the PDMS membrane that is between the valves and the channel underneath can be deflected. V1 and V2 seal the sensing channel in this way from the two main bypass channels when isolating a cell and/or switching the sample solution. V1 and V2 are partially lifted during data taking to allow fluid flow whilst preventing the cell from escaping. Sieve valve V3 is compressed to decrease the sensing volume and bring the cell closer to the electrodes for tunable sensitivity.

fringing electric field from a pair of planar electrodes is non-uniform and more sensitive to the presence of an insulating object the closer that object is to the electrodes[103]. A schematic of the current microfluidic chip is shown in Figure 2.4 featuring the new sieve valve (colored violet). But the fact that the sensitivity is increased when an object is closer means that the measurement produced by the planar electrodes will greatly depend on the position of the particle. Distance from the electrodes is not the only factor that can create variability, however, as cells that are asymmetrical, such as yeast, will affect the magnitude of the impedance pulse depending on its orientation. In order to mitigate this effect, the channel height was set at 20 μm so that the cells would sink farther away from the electrodes (as the device is upside-down

on the microscope stage and yeast has a density of 1.1 g/cm^3 while the aqueous solutions are essentially as dense as water) and thus make the measurement less susceptible to orientation-induced variations. While this height was chosen as a compromise between sensitivity and variability, it was determined only for the size of the yeast cells that were used. Different strains of budding yeast can grow to different sizes—haploids are smaller than diploids, for example—so one of the reasons for adding the central sieve valve was to make the volume sensor more adaptable. This would be especially necessary if bacterial growth were to be monitored. Another reason is that not all electrodes perform with the same quality, therefore a flexible channel height above the electrodes allows more devices to be useable since each can be calibrated individually (to be elaborated on later). The final reason is that by compressing the sieve valve and creating a narrower channel, the flow speed across the electrodes automatically increases by virtue of flow rate conservation. This means that the pressure regulators can operate on smaller pressure differentials to achieve the same desired flow speeds, making the dynamic flow reversals more stable and the flow speeds more consistent. This is important because precise flow control and flow speed have been shown to be governing factors in the reproducibility of impedance measurements[104]. However, the problem of variability due to position and orientation is not resolved by the addition of this sieve valve. A discussion on the measurement limitations and other aspects of the sensor's performance are detailed in subsequent sections.

2.2 Fabrication and Materials

The assembly of the microfluidic device relies on the microfabrication methods of photolithography and soft lithography, as discussed in Chapter 1 (detailed protocols for all the fabrication processes are found in the Appendix). But the elastomer that is used for the soft lithography has thus far not been discussed. It is a material known as polydimethylsiloxane (PDMS). This elastomer has been widely used and well documented in its applications for microfluidics, specifically due to several key advantages[105]. 1) as a liquid elastomer before being cured, it is able to replicate micron-sized structures with high fidelity; 2) it can be cured at relatively low temperatures (70-80°C); 3) it is optically transparent down to 280 nm; 4) it is

completely non-toxic and so is perfect for biological applications—it is even found in processed foods; 5) it is flexible and so can reversibly deform to make pumps and valves; 6) it is permeable to gases; 7) it is cheap and easy to work with; 8) and it can be easily bonded to itself or can be more strongly bonded to many substrates through plasma treatment. However, there can be problems depending on the nature of the application, as PDMS is inherently hydrophobic, has its own solvent compatibilities[106], and has been known to leach unpolymerized oligomers[107]. Therefore, care should be taken based on the circumstances of use.

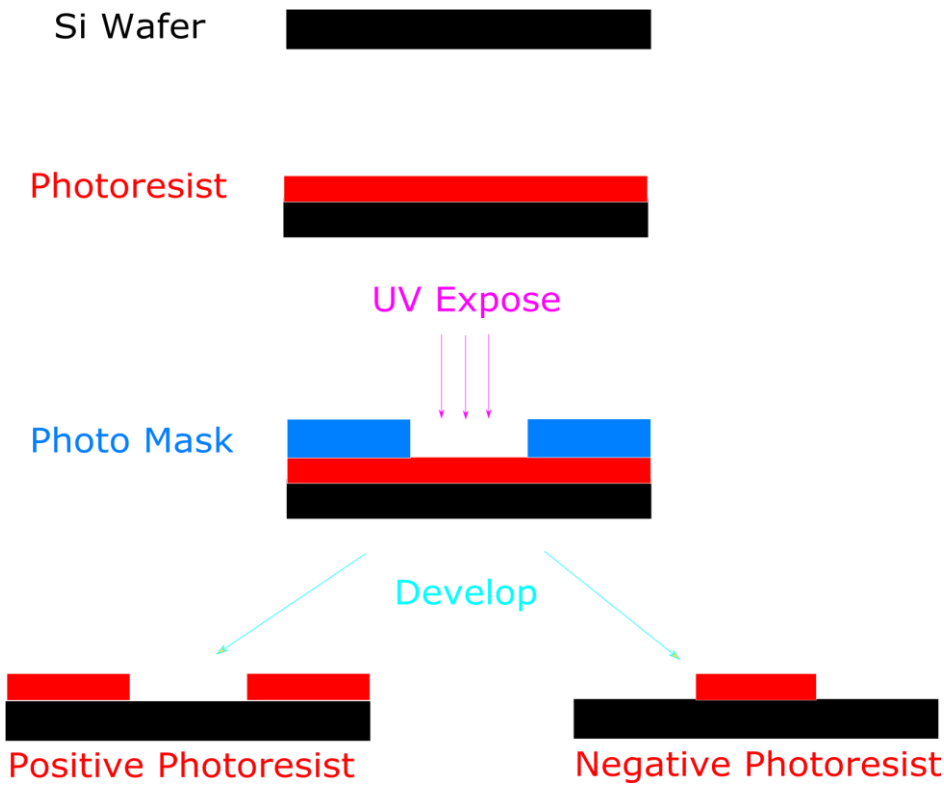

Figure 2.5 Silicon wafers serve as the typical substrates for photoresist. In the case of positive photoresist, the areas exposed to UV light become soluble to the developer. Conversely, negative photoresist becomes insoluble upon UV exposure. Photomasks intended for negative photoresist must be inverted (areas without features are black).

PDMS serves as the main body of the microfluidic chip, and is used in two layers. The multilayered soft lithography requires the use of two master molds, created using photolithography. One wafer is patterned with the positive AZ® photoresist and serves as the channel layer master; the second wafer is patterned with the negative SU-8® photoresist and

serves as the valve layer master. A diagram of this process is shown in Figure 2.5. The positive photoresist is used for the channel layer because it is able to thermally soften through a process known as reflow. This ensures that the original rectangular cross-section is rounded, a necessary step for the use of sieve valves.

To make the channel layer, PDMS is first created by mixing the siloxane base and the curing agent, then the mixture is placed under vacuum to remove the air, and finally the PDMS is spread over the channel master using a spin coater. The resulting thin layer of PDMS acts both as the walls of the channel and as the film that deforms in response to pressure from the valve chamber above. The valve layer containing such chambers is molded using the negative photoresist master. PDMS is cast directly onto the valve wafer, cured, and then peeled off. This block of PDMS is then plasma-bonded on top of the thin PDMS layer on the channel master. The bonded double-layer block is then cut and removed from the channel master, forming the main body of the chip. When this block is peeled off of the wafer, the space that was once occupied by the photoresist features will ultimately become the channels themselves. The bottom surface of the channel is the glass on which the electrodes are deposited. They are plasma-bonded together as well. Each assembly of the layers requires careful arrangement as well, and this is done using an aligner. Shown in Figure 2.6a are each of the layers in the assembled device. The thin PDMS layer that was spin coated over the channel master now serves as the membrane that is deformed downwards when the valves V1, V2, and V3 are pressurized. These types of valves are also known as pushdown valves. Just like the channel, the valves themselves are formed from hollowed spaces as a result of the molding process. They are filled with water in order to apply hydrostatic pressure on the thin PDMS layer below. The assembled chip is shown in Figure 2.6b.

A)

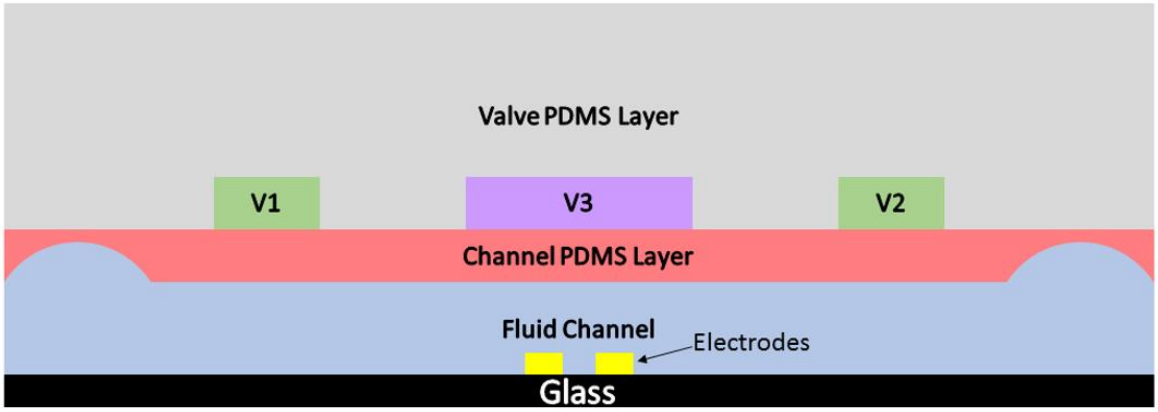

B)

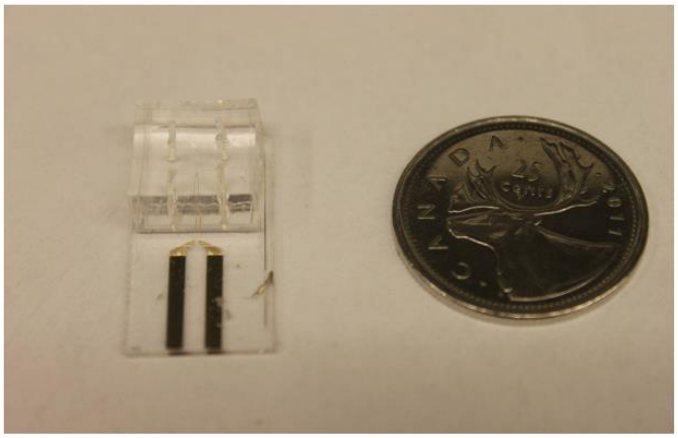

Figure 2.6 A) This shows a cross-section of the assembled device. The fluid channels are filled through the inlets shown in Figure 2.4. The rounded feature of the channels on each side show the cross-section of the bypass channels and is a result of reflowing the positive AZ photoresist, which is done to make pushdown valves more effective. B) The visible bulk of the PDMS block comes from the thick valve layer. Using biopsy punches, holes are made in the PDMS for the insertion of tubing into the 2 inlets, the 2 outlets, and all 3 valves. The column-like structures are the result of the biopsy punch.

To create the on-chip microelectrodes, thin film deposition was performed using electron beam evaporation. Electron beam evaporation is preferred over thermal evaporation because the heating is localized by the electron beam, thus keeping the sample cooler. This is necessary for maintaining the integrity of the photoresist that is used for patterning in the lift-off process. In addition, the localized heating means that any possible contaminants in the system will not be evaporated and deposited onto the substrate along with the desired metals. Glass is the chosen substrate because it is transparent, chemically inert, readily available in the form of microscope slides, and has a very suitable surface for plasma-bonding with PDMS. However, an adhesion layer is usually required because while metals bond well with each other,

not all bond well to glass[108]. Chromium (Cr) and titanium (Ti) are the two most common adhesion layer metals. In this work, a 5 nm adhesion layer was used. The main electrode layer is normally made using a noble metal. Gold (Au) is chosen in this work because it is at the bottom of the activity series and so should be very unreactive. It is also the third most conductive metal, which helps to minimize the electrodes' own impedance contribution. A 50 nm gold layer was used for the electrodes. An important point to note is that because gold is used, titanium is the preferred adhesion metal over chromium due to differences in electrode potentials. Since the application of the electrodes requires the presence of electrolytes (Coulter Principle), two metals with contrasting electrode potentials exposed to electrolytes will form a galvanic couple. In a galvanic couple, current flows internally between the metals and with the electrolyte solution. The more noble metal acts as the cathode and the less noble metal acts as the anode. This can lead to galvanic corrosion. Shown in Figure 2.7 is a pair of electrodes made from Cr-Au. They were exposed to various concentrations of aqueous NaCl during performance tests and the result was the loss of entire areas of the electrodes. In galvanic corrosion, the anodic metal is corroded, and since Cr is the less noble metal, its removal meant the loss of the adhesion layer. Titanium on the other hand has about half the difference in electrode potential relative to gold (~0.3 V Ti-Au vs. ~0.6 V Cr-Au), and so is the better adhesion metal of the two. However, this does not mean that Ti is ideal as there is still a gap between the electrode potentials; Ti is simply the most noble metal that adheres strongly to glass.

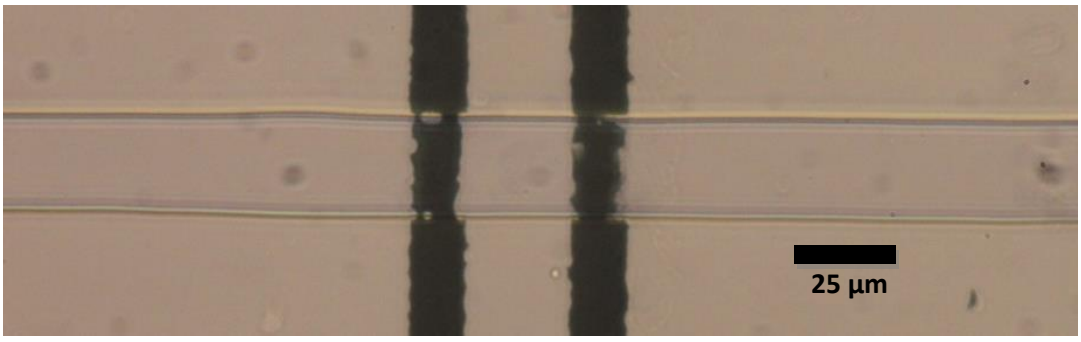

Figure 2.7 A bright field image taken in transmission mode. The electrodes are Cr-Au, 5 nm and 50 nm respectively, deposited using electron beam evaporation. Patches of the metal began to disappear after a few current measurements were made using varying concentrations of NaCl dissolved in deionized water (concentrations of 50 mM up to 1.5 M). This has not been observed with Ti-Au electrodes.

The electrodes are designed such that the sections spanning the sensing channel are each 20 µm wide while the inner edges of each electrode are separated by a distance of 30 µm. Such dimensions are patterned using two methods: the lift-off process and wet-etching (see Appendix for details). Lift-off uses photoresist to cover the areas of the substrate that the metals are not to be deposited on and exposes the areas where the electrodes are meant to be deposited. The shapes of the exposed areas therefore become the shapes of the electrodes. When the photoresist is developed, it lifts off the unwanted metal on top of itself, hence the name. This method is safer than wet-etching but was found to have a lower yield of approximately 20-40%. Lift-off is also more time-consuming, particularly the photolithography part. In an effort to improve the fabrication process, wet-etching was tested. This method deposits metals on the entire surface of the substrate and uses chemicals to etch away the excess metals, leaving only the areas meant to become the electrodes. Photolithography is used to pattern the geometry of the electrodes via a coat of photoresist placed on top of the deposited metals. This protects the metals from being etched top-down and acts as an umbrella that shapes the retained metal underneath. The gold is etched with aqua regia, a mixture of water, hydrochloric acid (HCl), and nitric acid (HNO_3). The particularly dangerous aspect of this entire process, however, is the etching of the titanium adhesion layer, as it requires hydrofluoric acid (HF). The HF must also be paired with something that can generate titanium dioxide, usually a peroxide compound. Titanium is consequently etched as the HF dissolves the oxide layer on top and while the peroxide regenerates it, repeating until the metal is gone. The yield for wet-etching was found to be at least 80% based on physical inspection—much better than lift-off. Unfortunately, electrical performance was mostly poor despite no apparent physical defects. The hypothesis was that the photoresist used to protect the metals from the etchants was not entirely removed. Many attempts to clean the surface using aggressive methods such as piranha, boiling acetone, oxygen plasma, as well as various voltammetric techniques[109] did not produce definitive results. Regrettably, this problem has not yet been resolved. And while electrodes can still be fabricated using lift-off, a solution to this would offer truly superior yield.

2.3 Experimental Setup

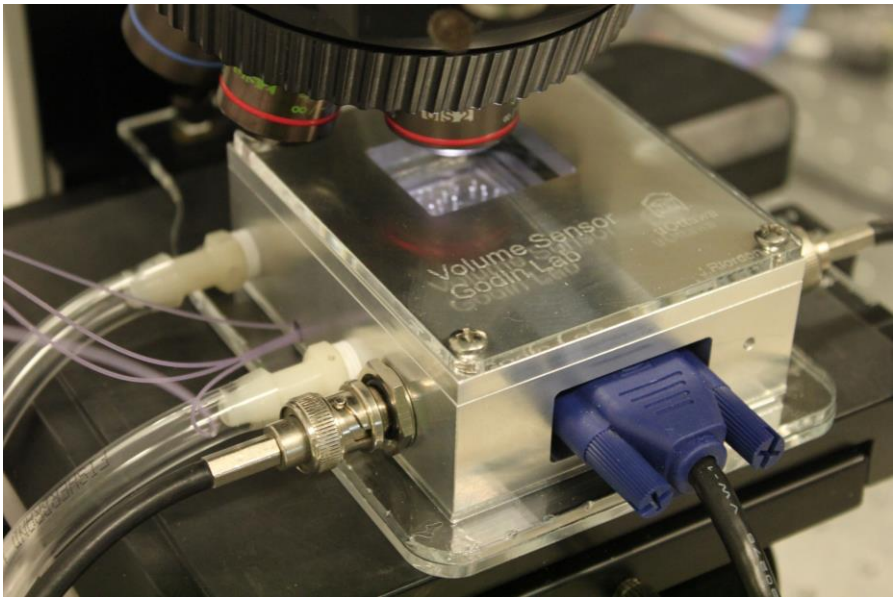

Figure 2.8 The aluminum block that houses the microfluidic chip and acts as a Faraday cage. The pair of clear tubing carries the water that heats the block while the purple tubing carries the actual fluid flowing into and out of the device. The vials that the purple tubes come from are next to the microscope and are hooked up to pressure regulators. Inside is a PCB that interfaces the BNC connectors to the microfluidic chip. The cables are linked to the external electronics. The VGA cable is for reading out the temperature monitored by a thermistor inside the block. (Reproduced with permission from the author[101])

As shown in Figure 2.8, the microfluidic chip is mounted inside a hollowed aluminum block that sits on the microscope stage. To attach the device, it is soldered upside-down to a PCB board located inside the aluminum block. The chip is maintained at 30°C during yeast experiments using an external water recirculator that pumps heated liquid through the aluminum block via tubing connected to the left side of the block. The recirculator itself is set at 32°C to account for the temperature drop as the liquid moves through the tubing to the microscope stage. BNC connectors on the left and right sides of the block allow for cables to connect the chip to the external electronics. Shown in Figure 2.9 is a schematic of the circuit used to conduct the impedance measurements. The function generator (Stanford Research Systems DS345) sends out an AC signal with a frequency of 100 kHz—changed from 50 kHz (to be elaborated on later)—and has an amplitude of 300 mV. The AC signal also has a DC offset of -300 mV (to be elaborated on later). This is fed to a unity gain low noise preamplifier (Stanford Research Systems SR560), which is set to DC coupling. The signal then goes to the microfluidic

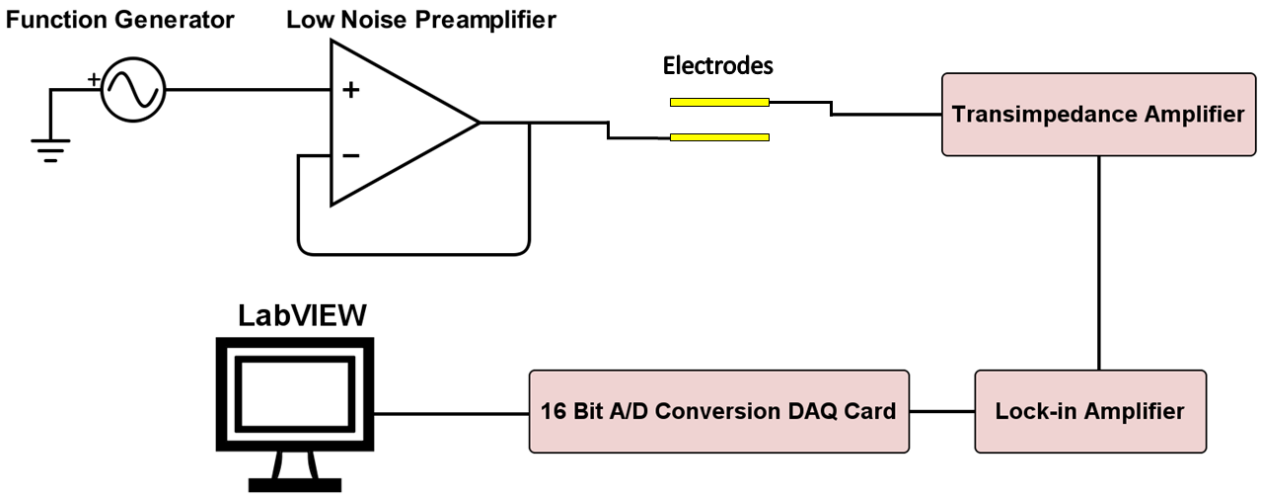

Figure 2.9 The electronics setup for the measurement system. An AC signal at 100 kHz is passed to a unity gain low noise preamplifier. This output is passed to the microfluidic chip, where the two electrodes are configured in series with each other, and the sensing volume impedance is between them. The measured output is converted to a voltage and amplified using a transimpedance amplifier. The signal frequency is isolated using the lock-in amplifier and then sent to a 16 bit National Instruments® DAQ card which is read by the LabVIEW® program.

chip via a BNC cable. The potential is applied to the first electrode and the output is received from the second electrode. The electrodes are grounded to the common wall ground through the BNC connection. The output signal travels through a BNC cable to a transimpedance amplifier (Keithley 428) that amplifies the signal by a factor of 10^4. This is then fed to a lock-in amplifier (Stanford Research Systems SR830 DSP) which filters out DC components and isolates only the driving frequency in order to reduce noise. The filtered signal is then acquired at 200 kHz using a 16-bit DAQ card (NI USB-6353). A LabVIEW program reads the digital output from the DAQ card and performs curve-fitting, data recording, and the control of two pressure regulators.

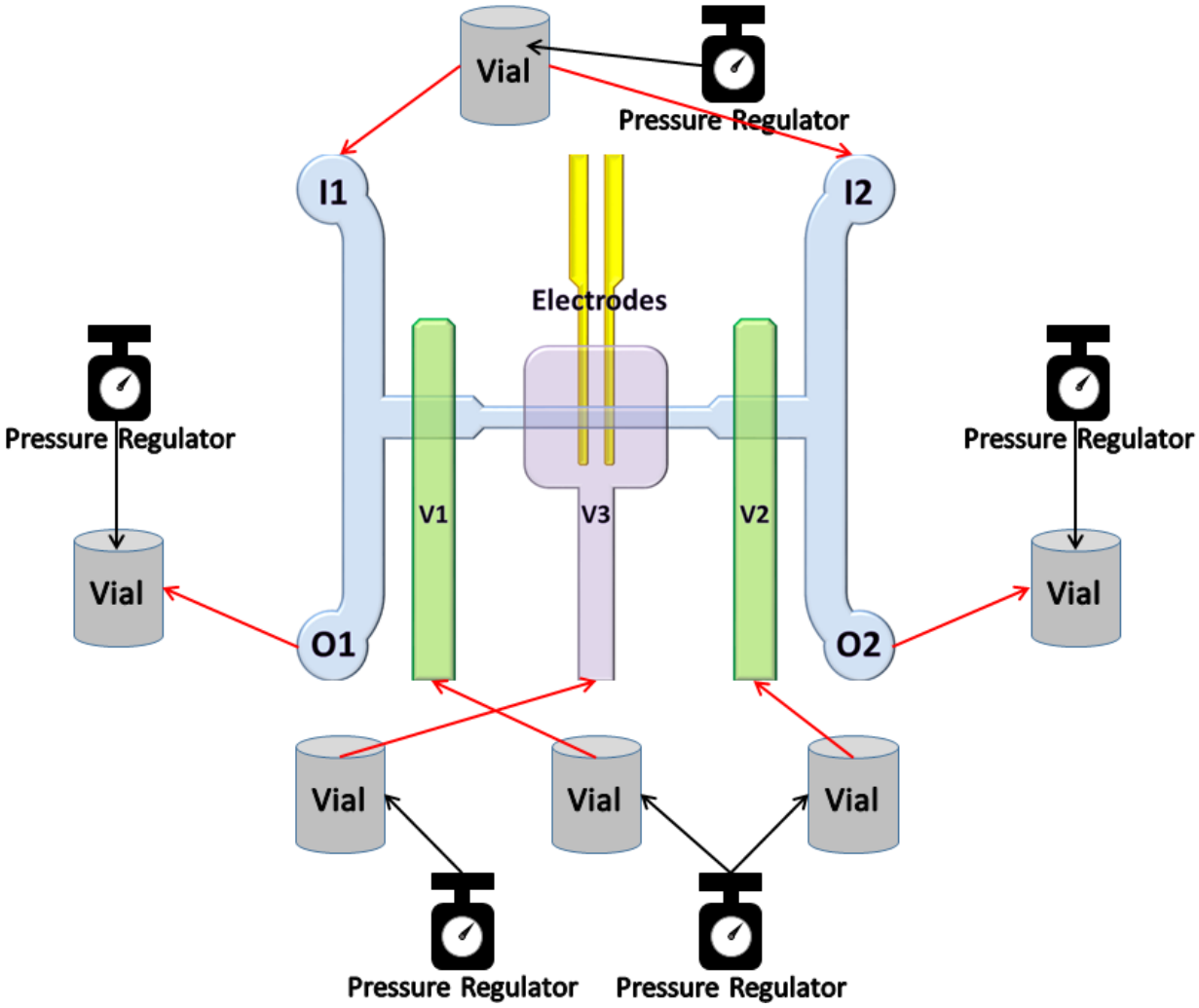

Figure 2.10 The red arrows indicate a tubing connection between the vials and the device. The inlets receive fluid from the same vial, the outlets expel fluid into their own vials, and water is pushed into the valves until they are filled and the air is pushed out. Pressure regulators receive pressurized air from the lab and are connected to the vials through a syringe tip in the cap. The tubing is also inserted into the vials through the cap. Only the two outlet regulators are computer-controlled.

Figure 2.10 depicts how the device is pressurized and where the fluids come from. There are 5 pressure regulators in total, 2 computer-controlled ones and 3 manual ones. The two inlets to the device are fed from the same vial and so are both pressurized using one manual regulator. During experiments, the inlets are held fixed at ~5 psi. The two outlets each empty into their own vials and so are individually pressurized using the two computer-controlled regulators. Their pressures change dynamically but are centered on about ~3 psi. The two valves used to the seal the sensing channel are controlled by a single manual regulator and are set to 35 psi when completely closed. When they are partially lifted during the experiment, the

pressure is set at 24 psi. The sieve valve over the electrodes is set to ~14.5 psi during experiments using a manual regulator. This value was determined through tests with beads and yeast cells, but it is a value that is subject to change depending on the performance of the device at hand and the application. For these pressure settings, a target transit time (the time the cell takes to flow past the electrodes) of 220-260 ms and a tolerance of 20 ms were set for the program based on trial and error. This was accomplished through the dynamic control of the outlet regulators via a feedback loop. And so by accounting for the movement range of the cell as it is shuffled back-and-forth under these settings, the upper limit on the diffusion time for a galactose molecule to reach the cell from the bypass channels was estimated to be ~2 minutes. This is an upper limit because Taylor-Aris dispersion[6] will augment the innate diffusion. Consequently, nutrient replenishment rates on this timescale should be more than sufficient for the yeast experiments, as they can last for several hours.

2.4 Calibration and Optimization

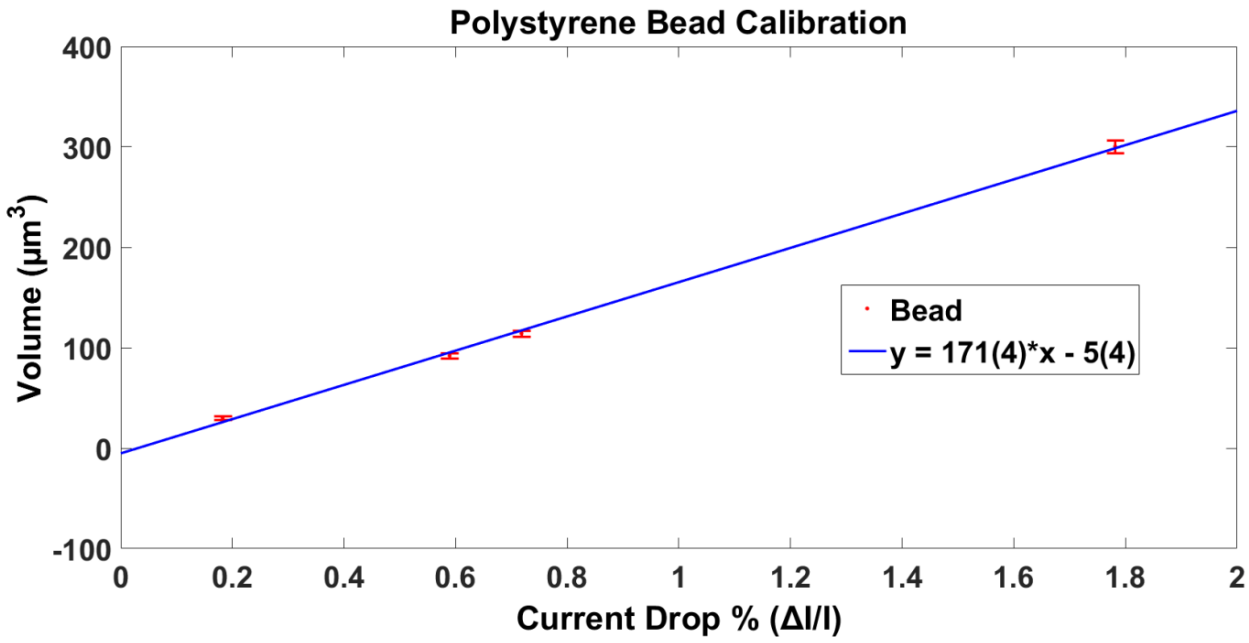

Figure 2.11 An example of a real calibration done for YPgal + 50 mM NaCl + 0.5% BSA (BSA is a biocompatible substance that helps to prevent the beads from sticking to the channel walls and to each other). Each red point represents one polystyrene bead size and is the average of roughly 10-20 minutes of data (a few hundred data points). The error bars are the standard deviations of each sample. The volumes for the known bead sizes are calculated and plotted with their corresponding current drop averages. A linear fit is performed to determine the calibration.

The impedance measurements are registered as current drop percentages. For each impedance pulse, a raw data point represents the change in current, ΔI, divided by the baseline current, I. In order to correlate this data to an actual volume, a calibration is needed. To do this, polystyrene beads or microspheres were purchased. They are highly spherical and have known diameters. Four bead sizes were used for the calibration; they had diameters of 3.81 μm, 5.67 μm, 6.02 μm, and 8.31 μm. Each sample was washed through three centrifugation cycles and suspended in the same solution used for the cells. A bead of each size was then trapped in the volume sensor and cycled over the electrodes for roughly 10 to 20 minutes. The data sets were averaged to produce one data point per bead size. This data is plotted and then fitted using linear regression, as shown in Figure 2.11. The equation for this line is then used to convert current drop measurements into volumes. It should be noted, however, that a calibration must be performed for each new device or solution as the calibration is only valid for the particular set of conditions that it was done under.

While a cell is electrically opaque at these frequencies, just like a bead, the calibration assumes that the surface charges on the bead and the cell are similar and that their effects on the overall impedance, relative to each other, are negligible. Obviously, the surfaces of these two objects are not the same as cell membranes have many protruding proteins and compounds are constantly being transported through the membrane. But this would only contribute a systematic error that does not affect the differences between volume measurements, which is what growth rates are concerned with. In addition, this error is actually quite insignificant as the computed volume corresponding to the initial size of single *S. cerevisiae* cells typically ranged from 20 to 30 μm^3. Assuming a spherical cell, this translates to a diameter of 3 to 4 μm, which is the correct initial size for single cells of budding yeast.

The main drawback of the calibration is the specificity. The two primary changes to the sensing conditions come from the channel height (through the sieve valve) and the salt concentration of the media being used. Both of these alter the impedance of the sensing volume and can therefore tune the measurement sensitivity. Thus it would be preferable to not have to individually calibrate every adjustment to these two factors. In the hopes of trying to

predict the changes to the amplitude of the impedance pulse for a given particle as the channel height or the salt concentration is varied, current measurements were done to evaluate the impedance of the sensing volume in response to these variations. The measurements were performed at 50 kHz and the current was found to change nonlinearly. While the trend was the same for all devices, the exact results varied among them. These observations were attributed to differences in electrode quality, PDMS stiffness, and most importantly, in the various impedance contributions. As discussed in chapter 1, the salt solution has capacitive impedance and the electric double layer at the electrodes gives rise to the polarization impedance. In addition, changes to the salt concentration will both affect the EDL capacitance[110] and alter the electrolytic conductivity in a nonlinear fashion[111]. While these difficulties forced the continued practice of individual calibrations, it did prompt further investigation into the choice of the signal frequency.

At a frequency of 50 kHz, the most dominant capacitive impedance in the sensing volume comes from the electric double layer at the surface of the electrodes. To characterize this, two different concentrations of NaCl dissolved in deionized water were used to measure the baseline current at four frequencies: 10 kHz, 25 kHz, 50 kHz, and 100 kHz. The results are shown in Figure 2.12. As can be seen, the current increases nonlinearly with frequency towards a plateau. The transition from 50 kHz to 100 kHz at 50 mM NaCl resulted in a miniscule current increase (0.6827 to 0.7022 μA) while the same transition at 100 mM resulted in a more appreciable increase (1.2409 to 1.4207 μA). This makes sense because a higher salt concentration will worsen the polarization impedance caused by the electric double layer and will therefore require a higher frequency to make the effect negligible. This is supported by the fact that a doubling of the salt concentration at 100 kHz produces a much greater increase in the measured current than at 10 kHz, as the electrolyte impedance is eclipsed by the polarization impedance at the lower frequency. So by switching to a higher driving frequency, the measurement will become more sensitive to cell size. This agrees with what was discussed in chapter 1. However, the lock-in amplifier has a cutoff frequency that is slightly above 100 kHz, thus placing a limit on how high the signal frequency can be. Consequently, the function generator was set to operate at 100 kHz.

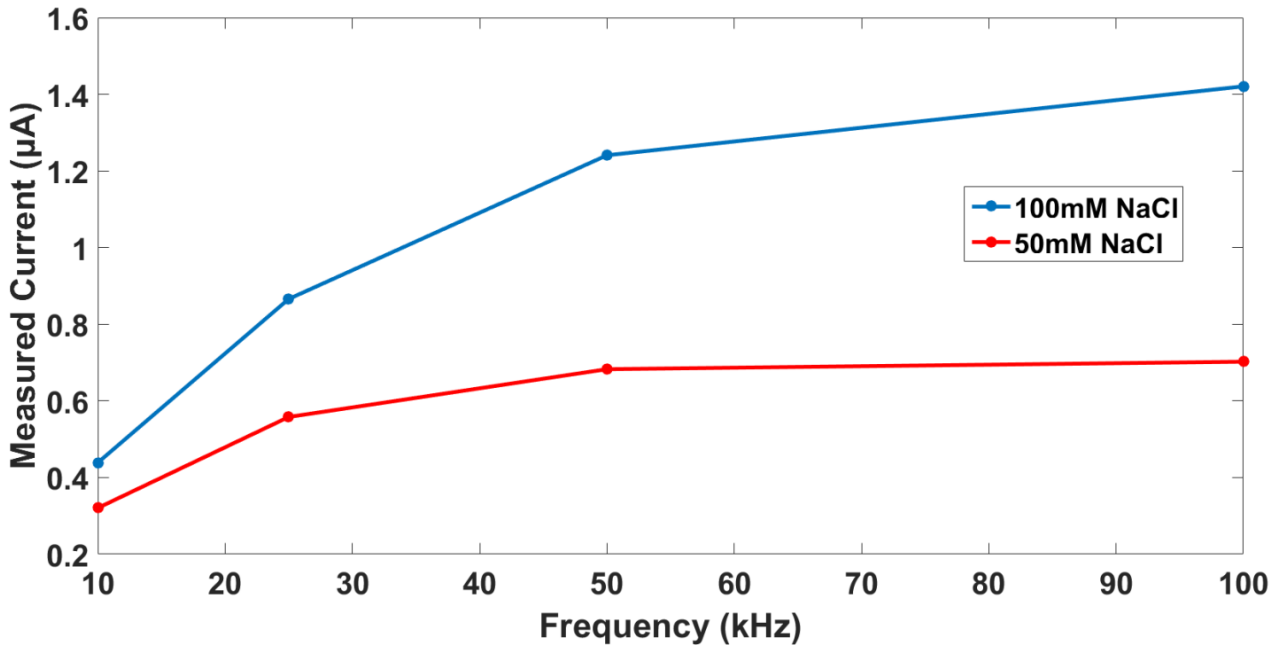

Figure 2.12 This graph shows the frequency dependence of the measured current and therefore of the sensing volume impedance. The solutions used were simply NaCl dissolved in deionized water. Each data point is the average of ~3000 data points acquired from a steady baseline current. These measurements were made without modifying the inherent channel dimensions of 25 μm x 20 μm (width x height). What is also apparent is that when the concentration is doubled, the change in current depends on the frequency used. For example, at 10 kHz, a doubling in the concentration does not result in a doubling of the measured current, whereas at 100 kHz, the measured current is more than doubled.

Another way to reduce the electrode polarization impedance is to increase the microscopic surface area of the electrodes[112]. A characteristic of thin film metals is that regardless of the deposition method, pores always form in the film[113]. While porosity is usually undesirable as it promotes corrosion and cracks from internal stresses, an auspicious side-effect of pores is that they increase the effective surface area of the metal. Naturally, this has been of great help to the gold electrodes in the volume sensor. However, this can be further improved through the use of platinized platinum electrodes[114]. Platinum, just like gold, is extremely unreactive and can also be microfabricated in the exact same ways that gold can be. The main benefit is that platinum electrodes can be coated with what is known as platinum black, a fine powdered form of platinum. This process is known as platinizing platinum. The platinum black coating is very rough and porous; as a result, it greatly increases the effective surface area of the electrodes and is the best way to reduce electrode polarization impedance materialistically. While the coating process does require a bit more work than the

use of gold, it is a feasible alternative for improving sensitivity to size. In fact, platinum black electrodes have already been integrated into microfluidic devices[61][64][115][116]. One final thing to note is that the surface electrochemistry would be different compared to shiny platinum and gold, especially since platinum black is often used as a catalyst. This could have additional benefits or flaws, and therefore deserves consideration.

2.5 Electrode Discoloration

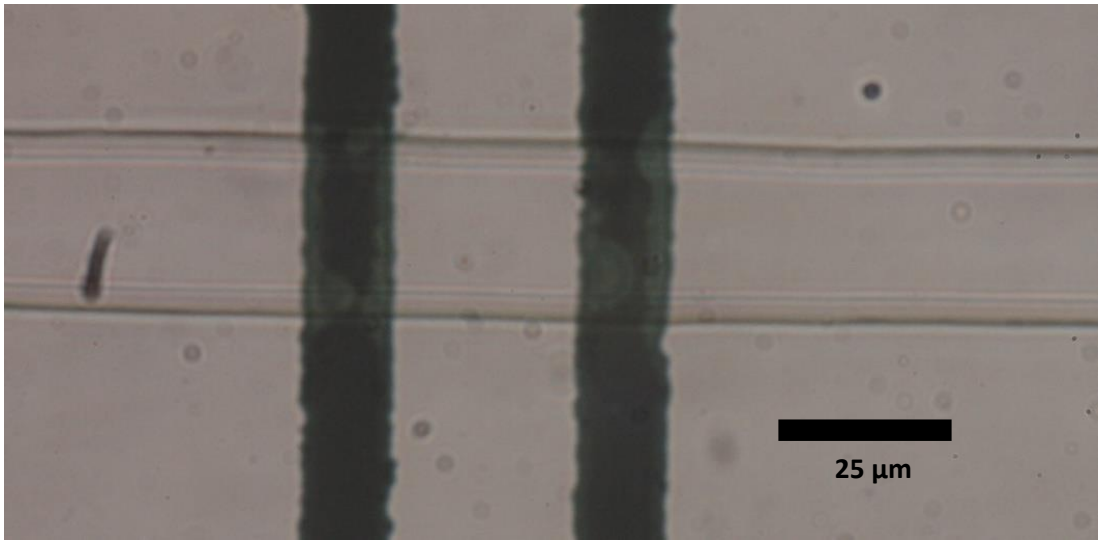

Figure 2.13 Bright field transmission mode image of the electrodes. The side of the electrodes facing the objective is the side that is adhered to the glass. The device is inverted on the microscope stage so the electrodes are actually on the ceiling of the channel. Consequently, the surface of the electrodes exposed to the fluid is not being viewed. This means the discoloration is seen *through* the electrodes.

An unfortunate electrochemical effect that has been observed is the discoloration of the electrodes after use in the presence of electrolytes. Under the microscope, a bright field transmission mode image of a thin gold film will appear green. For a thickness of 50 nm, the unaffected regions of the electrodes have a very dark green color, but the discolored regions are a much lighter shade of green, as shown in Figure 2.13. The sections of the electrodes exposed to the channels suffered this effect, so it must have been related to the presence of the electrolyte solution. A key point is that the bottom side of the electrodes is viewed in the image. This is because the device is upside-down on the microscopic stage where the illumination comes from below and the objectives are above. Thus the side of the electrodes exposed to the fluidic channel is facing downwards and the side adhered to the glass is facing

upwards at the microscope objective. This means that the discoloration is seen as the light passes through the electrodes. If the gold were to become thinner, it would certainly appear a paler green. This therefore implies that material was most likely being lost, resulting in thinning of the metal. Despite the fact that gold is normally inert, these signs indicate electrochemical oxidation, as it only occurred after a potential was applied in the presence of electrolytes. The inherent pores in the metal probably facilitate this process as well by exposing large surface areas within the bulk structure. A remedy would be to lower the amplitude of the applied potential, but this would greatly reduce the signal-to-noise ratio of the measurement. Instead, a DC offset to the AC potential was introduced to see if one of the electrodes could be spared from oxidation. In order to ensure that the oxidation potential at one electrode was never met, the driving signal was given a -300 mV offset with its 300 mV amplitude.

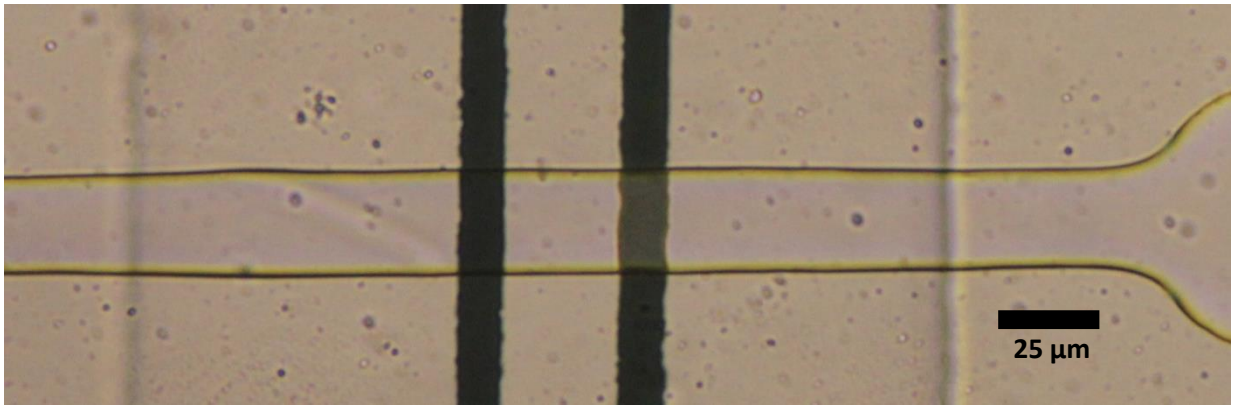

Figure 2.14 Only one of the electrodes became pale green, even after very prolonged and repeated use. The paler electrode is the one connected to the output and is the more positive electrode (anode) given the conditions set by the function generator.

As shown in Figure 2.14, only one of the electrodes appears paler. The electrode that was spared was the one connected to the function generator side (input) and the electrode that was affected was the one connected to the lock-in amplifier side (output). Because of the DC offset that is applied, the more negative input electrode acts as the cathode and the more positive output electrode acts as the anode. Since the electrolyte solution is predominantly NaCl, the presence of chloride could yield the following oxidation reaction at the anode:

$$\mathrm{Au(s)} + 4\mathrm{Cl^-(aq)} \rightarrow \mathrm{AuCl_4^-(aq)} + 3\mathrm{e^-}$$

Interestingly, the electrochemical reactions did not appear to have a pronounced effect on the volume measurements, and long term use of a pair of these electrodes under the DC bias continued to produce reliable data. This could be explained by the fact that the electrode was still conducting and that the oxidation did not appreciably increase the polarization impedance or the electrode's own impedance, so the measurement was still sensitive to the ionic displacement by a cell. However, the ultimate lifespan of the electrodes was probably reduced by these reactions. Thus it may be worth investigating the electrochemical response of platinum or platinized platinum, as their electrode potentials and electrochemistry will be different. But for the moment, it seems that this phenomenon can be coped with.

2.6 Measurement Limits and Suggested Improvements

As was stated in section 2.1, the primary source of error in the volume measurement comes from the position and orientation variations of the cell. Shown in Figure 2.15 is an

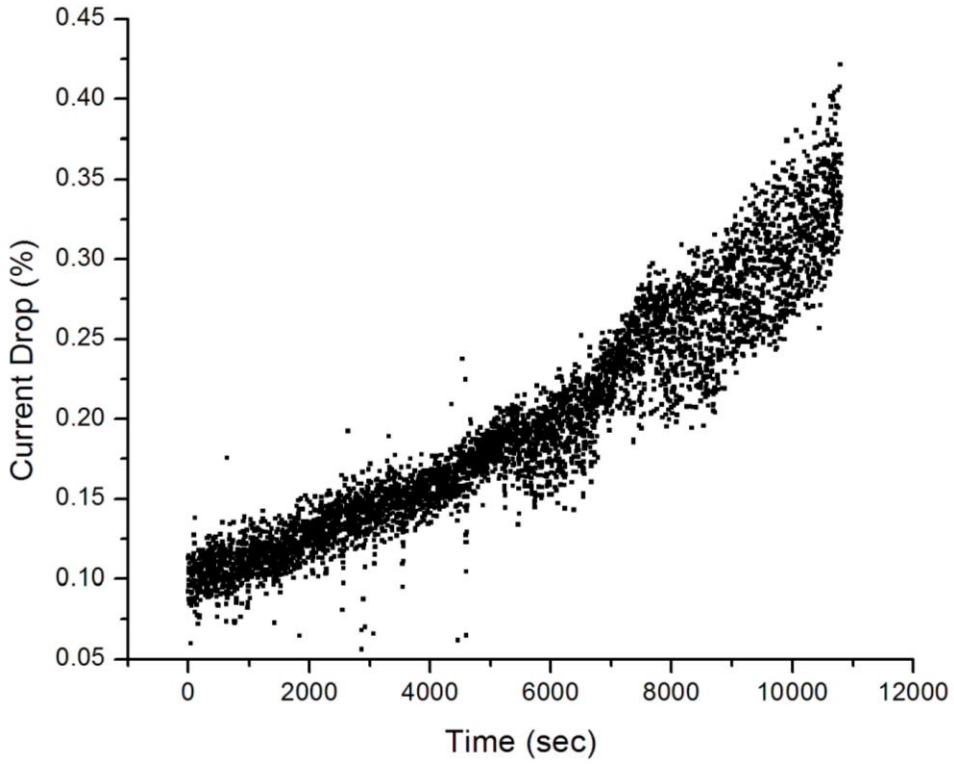

Figure 2.15 Raw data of a yeast growth curve. The spread in the data shows the inherent variations caused by changes in position and orientation. The effect is greater at later times when the mother cell has one or two buds attached, creating a highly asymmetrical shape that exacerbates the data spread.

example of the raw data taken during a growth experiment. As can be seen, the band of data points gradually widens as time goes on. Initially, there is only a single cell, which is approximately spherical, and so the error bar is smaller. But as buds begin to emerge, the cell cluster grows larger and more asymmetrical, resulting in greater discrepancies due to variations in position and orientation. This is because the amplitude of the impedance pulse will differ depending on how a yeast cell flows through the non-uniform electric field that arises from the coplanar electrode geometry, as illustrated in Figure 2.16. The closer the cell is to the electrodes, the denser the field lines are and the more sensitive the measurement becomes to position and orientation. For this reason, the height of the sensing channel was deliberately made to be 20 µm so that the cell would sink away from the electrodes when the device was mounted upside-down. But in order to better address this problem, either the electric field must be made more uniform or the position must be controlled.

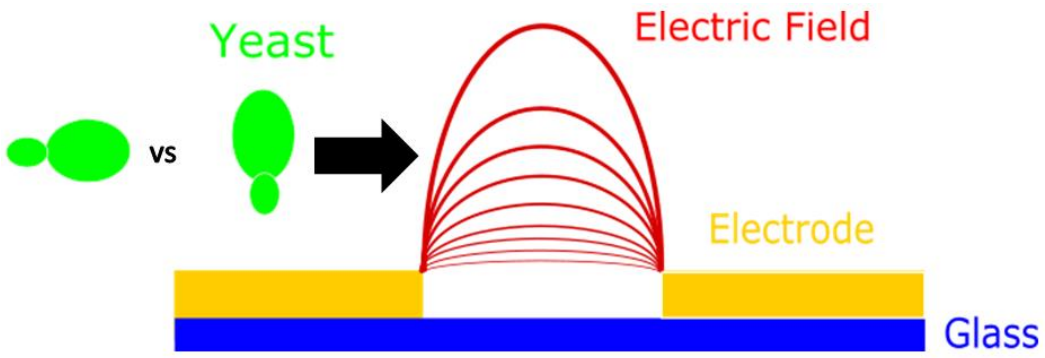

Figure 2.16 If a cell passes through where the fringing field lines are close together, the measurement will be more sensitive to position and orientation. If the cell is farther away from the electrodes, the measurement will be less sensitive to the size but also to the variations. This non-uniform field is due to the coplanar electrode geometry. Budding yeast tends to roll and tumble, accentuating the variations.

To create an electric field that is more homogeneous and symmetrical, the electrode geometry must be altered. Simulations have shown that a parallel electrode configuration is superior and would be able to produce such a field[117]. While microfluidic impedance cytometers have been constructed using parallel electrodes[55], the channels of these devices were made of glass, which greatly facilitated the deposition and assembly of 3D electrodes. Fluidic channels formed using PDMS, however, cannot integrate the parallel electrode geometry as easily. Three methods that have been suggested for fabricating parallel metal

electrodes in PDMS channels appeared applicable to the volume sensor. The first involves bonding bismuth alloy microspheres to the channel walls[118], the second uses ion implantation to deposit gold electrodes onto an exposed PDMS substrate[119], and the third uses UV-activated chemical adhesives to pattern gold directly in the flow channel[120]. Unfortunately, the actual implementation of these methods for the device is not a trivial matter and would still require significant labor to evaluate their long term feasibilities and efficacies.

The second way to reduce the measurement error is to keep the simplicity of the 2D planar electrodes and to control the position of the cell within the fluid channel instead. This is best accomplished through the use of acoustic forces. In fact, a microfluidic Coulter counter has already applied this to focus particles for better impedance sensing[121]. This particular device used glass channels and installed piezoelectric motors on the walls to generate bulk acoustic radiation pressure in two dimensions. This created a standing pressure wave within the channel that would force the particles to migrate to the pressure nodes. The drawback to this is that, again, glass is used to make the channels, thus forfeiting the crucial benefits of PDMS, one of which is the essential ability to fabricate valves. Fortunately, there is still a way in the form of surface acoustic waves (SAW). SAWs propagate along the surface of an elastic solid and decay exponentially with depth into the substrate. When the waves reach the solid-liquid interface at the channel, they 'leak' into the fluid at the Rayleigh angle and exert acoustic radiation pressure[122]. The subsequent force on a compressible sphere, which could be a cell, was studied in a seminal paper on the subject[123]. SAW has been applied to microfluidics in many ways[124], but the application of greatest interest to Coulter counters is particle focusing, as was explained earlier. A study demonstrated that standing surface acoustic waves (SSAW) could be produced in a PDMS microfluidic channel to perform the same role as bulk acoustic forces[125]. Shown in Figure 2.17 is a diagram of this from the publication. SAWs can be generated by electromechanical oscillations induced through the use of interdigital transducers (IDTs) patterned on a piezoelectric substrate. The frequency employed and the dimensions of the IDTs must both be chosen carefully to shape the standing wave in the channel. But the advantage of this method is that the fabrication steps are exactly the same as those for making electrodes. In fact, IDTs are basically electrodes in every way except function. They can be

microfabricated using the same thin film deposition and photolithography techniques. And to permit the creation of SAWs, the substrate that the electrodes and IDTs are deposited on simply needs to be changed from glass to a piezoelectric one, such as lithium niobate ($LiNbO_3$). Nonetheless, it should be noted that this is by no means a quick fix either, and would also require a fair amount of effort to realize. Overall, the best ways to improve the volume measurement are parallel electrodes and position control.

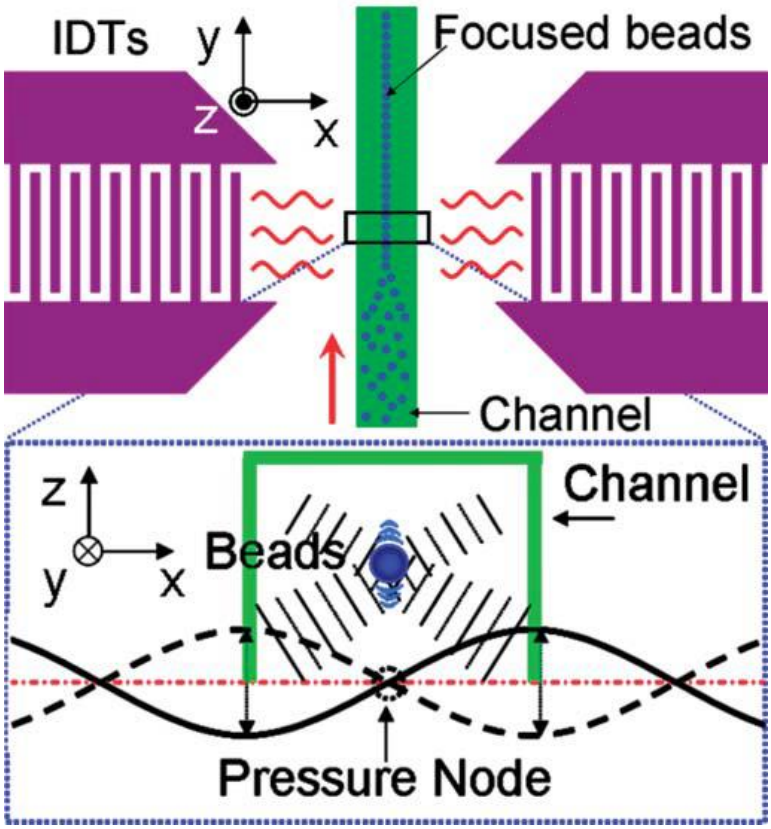

Figure 2.17 Using two interdigital transducers, a standing surface acoustic can be created that forces particles to stay at the pressure minima. The substrate was made from a lithium niobate wafer. (Reproduced with permission from the Royal Society of Chemistry[125])

2.7 Yeast Cultures

The *S. cerevisiae* strain used for the multidrug resistance study was BY4741: PDR5-yEGFP-KanMX. It was created by Afnan Azizi and modified from the parent strain BY4741 with genotype: S288C[a]: *MAT*a; *his3Δ1*; *leu2Δ0; met15Δ0*; *ura3Δ0*. Frozen stocks were stored at -80°C

and streaked onto an agar plate to act as a source for culturing. The plates were stored in the refrigerator and replaced every 2 months.

The main solution used in the preparation of all others was yeast extract peptone galactose (YPgal) which consisted of 2% w/v yeast extract, 4% w/v bacteriological peptone, and 2% w/v galactose, dissolved in DI-H_2O. For on-chip measurements, 50 mM NaCl and 0.5% w/v bovine serum albumin (BSA) was added to YPgal, and represents the regular media environment in this study. Cycloheximide was added to YPgal with 50 mM NaCl and 0.5% BSA to form the drugged environment in this study, but just YPgal plus cycloheximide was used for culturing.

For the single-cell growth experiments, cells were cultured in YPgal from a frozen stock and incubated for up to 24 hours at 30°C. From stationary phase a dilution was made and allowed to grow overnight into log-phase (exponential phase), to an OD_{600} of 0.1 to 0.4. Low-expressing cells used in the experiment were taken from this culture. Cultures to be used for selecting high-expressing cells were prepared from a vial of cells in log-phase, such as the one the low-expressing cells were taken from. Then three serial dilutions were made over 72 hours. Each was incubated overnight and allowed to grow to an OD_{600} of 0.1 to 0.4. The first dilution was dosed with cycloheximide to a concentration of 0.05 μg/mL. The second dilution raised the concentration to 0.065 μg/mL, and third dilution raised the concentration to 0.08 μg/mL. This serial increment was done to induce PDR5 transcription but without the shock of starting the cells at the experimental concentration of 0.1 μg/mL.

3. Measuring Fitness in Yeast Multidrug Resistance

This chapter covers the application of the volume sensor in evaluating the fitness of two phenotypes relating to yeast multidrug resistance in order to determine if this phenomenon is a case of bet-hedging. The following sections come from the majority of a currently unsubmitted manuscript and are wholly written by the author. The introduction will be altered with input from the other authors, but the message will remain the same. The Material and Methods section is excluded because the portions relating to the author's work have been covered in Chapter 2. Figure 3.1 in the Results section will not appear in the final publication, but serves as the established evidence for the bimodal expression of the PDR5 gene, originally discovered by Afnan Azizi (Figure 3.1A is reproduced with his permission)[126]. Aspects intended for publication by the coauthors of the manuscript are not included.

3.1 Introduction

Multidrug resistance (MDR) in cells is a cause of great concern in human health. MDR in bacteria was recognized early on[127] and has risen to become a contemporary problem facilitated by the continued evolution of mechanisms granting MDR[128]. The potential epidemic threat of dangerous MDR strains has also been aggravated with widespread misuse and overuse of antibiotics[129]. This issue faces additional difficulties from declining pharmaceutical production of new and effective drugs[130]. But the challenges of understanding and overcoming MDR are not confined to bacteria alone; fungi, including those from the infectious genus *Candida*, have also evolved mechanisms for multidrug resistance[131]. However, most salient of all eukaryotic MDR is that found in cancer, and is the main cause of failure in chemotherapies[132]. The mechanisms are varied, including mutations and epigenetic changes[133], but transmembrane efflux pumps in particular have been highlighted as a major root of MDR in cancer[134][135]. Cancer stem cells, for example, are known to have inherent drug resistance[136] and to express high levels of efflux proteins[137].

Unlike specific mutations, the functions of efflux pumps are not limited to granting MDR. Of all identified efflux pumps, the primary group is the ATP-binding cassette (ABC)

transporters superfamily that utilize ATP hydrolysis to pump substances across the cell membrane[138]. This large family of transporters is crucial to cell function and is responsible for conferring the efflux-mediated multidrug resistance phenotype observed[139]. ABC transporters are highly conserved and found in not just *Eukarya* but also in *Bacteria* and *Archaea*[140]. In cancer, the ABC transporter most commonly recognized and studied is P-glycoprotein[141], the product of what is now called the MDR1 gene. This has led to efforts in targeting these transporters to improve chemotherapy efficacy[142].

In the model eukaryote *S. cerevisiae*, multidrug resistance has also been identified, arising from the action of ABC transporters encoded by a gene known as PDR5[143]. PDR5 is a part of the PDR (pleiotropic drug resistance) network[144] which consists of a host of transcription factors that control the expression of the principal MDR gene of interest, PDR5, as well as other genes encoding ABC transporters[145]. Here we present a new discovery of two distinct levels of transcriptional expression of the PDR5 gene in an isogenic strain of budding yeast. Unique to this discovery is that phenotypic heterogeneity in multidrug resistance amongst isogenic eukaryotes has never been reported before to our knowledge. In contrast, it has been shown that for clonal bacteria growing in a homogeneous environment there exists a small group of stochastically realized persister cells[146] that are in an arrested growth state and do not die off exponentially under antibiotic treatment[147]. When the antibiotic is removed, these surviving cells can switch to the regular fast-dividing state and proliferate. This antibiotic resistance arising from a clonal bacterial subpopulation with its own phenotype is an example of the evolutionary theory known as bet-hedging[148].

Bet-hedging is a survival strategy in which isogenic populations 'hedge their bets' through risk-spreading whereby the resulting phenotypic heterogeneity maximizes the geometric mean fitness of the population across environments at the expense of arithmetic mean fitness[149]. This means that each phenotype confers a different fitness depending on the environment, granting the overall population better plasticity. Bet-hedging is thought to have evolved as a means of coping with unpredictably changing environments where one phenotype is better adapted for a particular condition than another[150]. While there is some

debate regarding the scope of criteria needed in order to qualify as bet-hedging, the general requirement is that the phenotypic heterogeneity must affect fitness and that the phenotypes must grant different fitnesses depending on the environment[151]. A better understanding of the mechanisms behind bet-hedging will grant valuable insight into gene regulation, systems level behavior, and the pathology of drug resistance from microbes to cancer cells.

Here we investigate the phenotypic bimodality of PDR5 expression with flow cytometry and spot assays, and use a microscopy-integrated microfluidic cell impedance sensor with media exchange[99] to measure the fitness of individual cells. To help distinguish between the two expression levels, we integrated yeast-enhanced green fluorescent protein (yEGFP) directly downstream of the gene sequence. To evaluate the fitness of each subpopulation in normal and cytotoxic conditions, we employed our microfluidic device to trap, image, and quantify the volumetric growth rate of single cells with on-chip variation of their environment. These results present the first case of bet-hedging in eukaryotic multidrug resistance.

3.2 Results

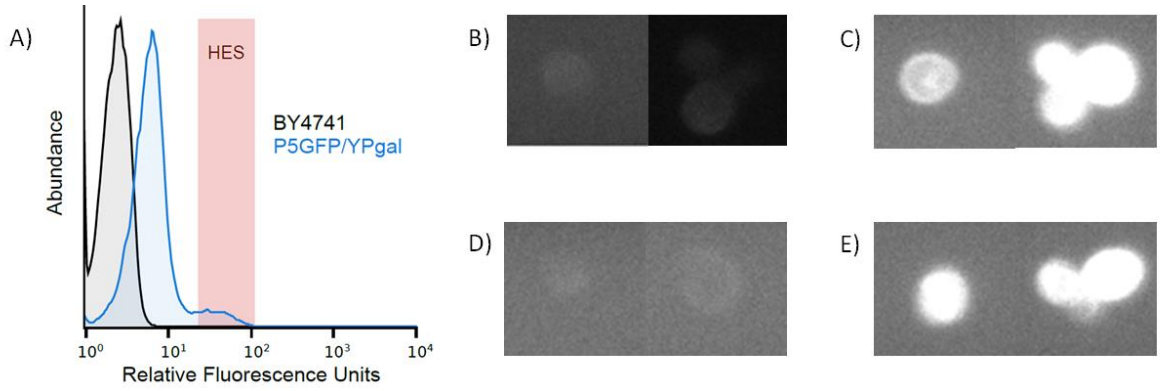

Figure 3.1 A) Flow cytometry analysis of the parent strain population BY4741 and the GFP enhanced strain in blue. There is a small peak in the fluorescence corresponding to the small subpopulation of HE cells (© Afnan Azizi[126]). B-E show sample images of GFP fluorescence intensity taken at the beginning and the end of their respective experiments. These were done to ascertain the phenotype of the cell at the start (left image in each pair) and to see if that state changed at the end (right image in each pair). The brightness and contrast settings are the same for all images. B) LE cells grown in regular media. C) HE cells grown in regular media. D) LE cells grown in cycloheximide. E) HE cells grown in cycloheximide.

Using flow cytometry, we characterized the distribution of GFP fluorescence intensity for the population and confirmed bimodality in the expression of PDR5, as shown in Figure

3.1A. The rarer high-expressing (HE) subpopulation exists minimally at ~1% while the dominant low-expressing (LE) subpopulation exists at ~99%. We therefore demonstrated phenotypic heterogeneity in an isogenic strain of yeast—a requirement for bet-hedging.

In order to evaluate the fitness of single cells from the minority HE subpopulation, cells were cultured over three days in regular media dosed with cycloheximide. We found that the HE state could be induced in this way to increase the number of cells exhibiting a high level of PDR5 expression since the transcription factor PDR1 is known to bind to drugs and then induce upregulation of PDR5[152]. Cells were flowed into the microfluidic device in the media they were cultured in, a target was then trapped in the middle sensing channel and the sieve valves were closed to seal it off from the main flow channels. A fluorescence image was then captured to ascertain the expression level, as shown in Figure 3.1. The inflowing fluid was then changed while keeping the trapped cell in the sensing region, to either regular media with 50mM NaCl as the regular media environment or this same solution spiked with 0.1µg/mL cycloheximide as the drugged environment. The device was thoroughly flushed with the new solution and the valves sealing the central channel were partially lifted so that the fluid could be shuffled back and forth until the trapped cell was also immersed in the changed media. With automated pressure control, the cell was cycled over the electrodes during the experiment, each time generating a drop in the current proportional to the cell volume by way of the Coulter Principle[56]. A fluorescence image was also made at the end of the experiment to evaluate the final expression state.

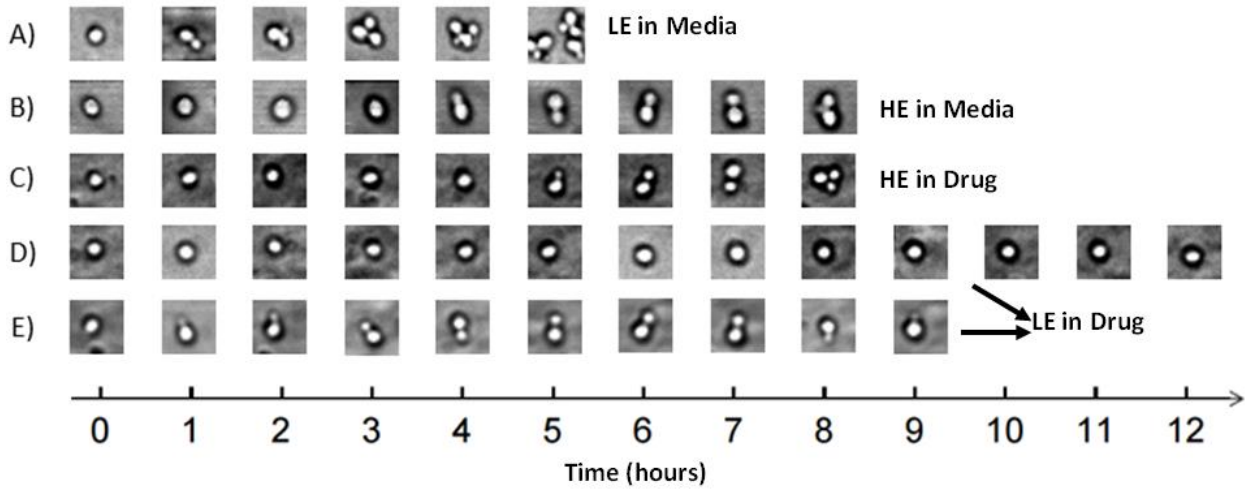

Figure 3.2 The above are sample time-lapsed images from the beginning to the end of each respective experiment. A) LE cell in media. B) HE cell in media. C) HE cell in cycloheximide. D) LE cell in cycloheximide that was not close to division at the start. E) LE cell in cycloheximide that began division at the time cycloheximide was introduced, however shrinking of daughter occurred later resulting in unsuccessful division.

Concurrently, time-lapsed images of the cells were taken over the course of the experiment to observe the time between budding events. The estimate of the time between the emergence of the first and second daughters is an approximation of the doubling time and reproductive rate, the means of which are shown in Table 1. In Figure 3.2, sample images for each experimental category provide an outline of the timescales of reproduction. LE cells in media display the greatest absolute fitness as depicted in Figure 3.2A, reaching a total of 8 cells after 5 hours, a stark contrast to their growth in cycloheximide. The HE cells, while lower in fitness compared to the LE cells in media (Figure 3.2B), are resilient to the shift into a cytotoxic environment, and, as seen in Figure 3.2C, growth is not significantly affected. We include two categories, as shown in Figure 3.2D and 3.2E, for LE cells grown on-chip in the drugged environment as there were two distinct observations. The first (Figure 3.2D) was no division at all within the timeframe of the experiment and the second (Figure 3.2E) was an observed emergence of the first daughter followed by death later on with shrinking of the bud.

Typical volumetric growth curves are represented in Figure 3.3A. LE and HE cells evaluated in regular media are shown to provide a comparison of their relative growth rates under normal conditions. All tabulated growth rates were quantified from the raw data via

analysis using MATLAB®. To estimate the growth rates, we used linear regression to compute the slopes. One such slope is the volumetric growth rate for the single-cell phase; the tabulated means appear in Table 1. However for some trials, the mother began with a daughter or produced one shortly thereafter, thus leaving an insufficient amount of data for the single-cell phase. For this reason, we also include a growth rate corresponding to just after the emergence of the first daughter, delineated as 'Collective Growth Rate with 1 Bud' (see Table 1 and Supplementary), and is extracted from the fit shown by the green line in Figure 3.3A. This captures the growth rate leading towards mitosis from just after entry into the S phase, when the collective growth rate is measured to be the greatest. And since cycloheximide is a eukaryotic translation inhibitor, this rapid growth stage should be particularly sensitive to it. But following this is a negative change in the slope, as shown by the yellow fit in Figure 3.3A, despite there still being only two cells. This is due to the slow down as the mother proceeds through mitosis and back into the G1 phase, and it is excluded from data consideration. As shown in Table 1, the way the mean collective growth rates compare with one another is consistent with the way the mean single-cell growth rates compare with one another. However, for the LE cells in the drugged environment, we observed a unique event for the cells that were able to bud at the onset of the experiment. After a period of growth, the daughter abruptly shrinks and continues to do so over time while the mother continues to grow. This is illustrated in Figure 3.3B. We also performed a fit for the slope during this phase for the cases where it was observed (see Table D in Supplementary).

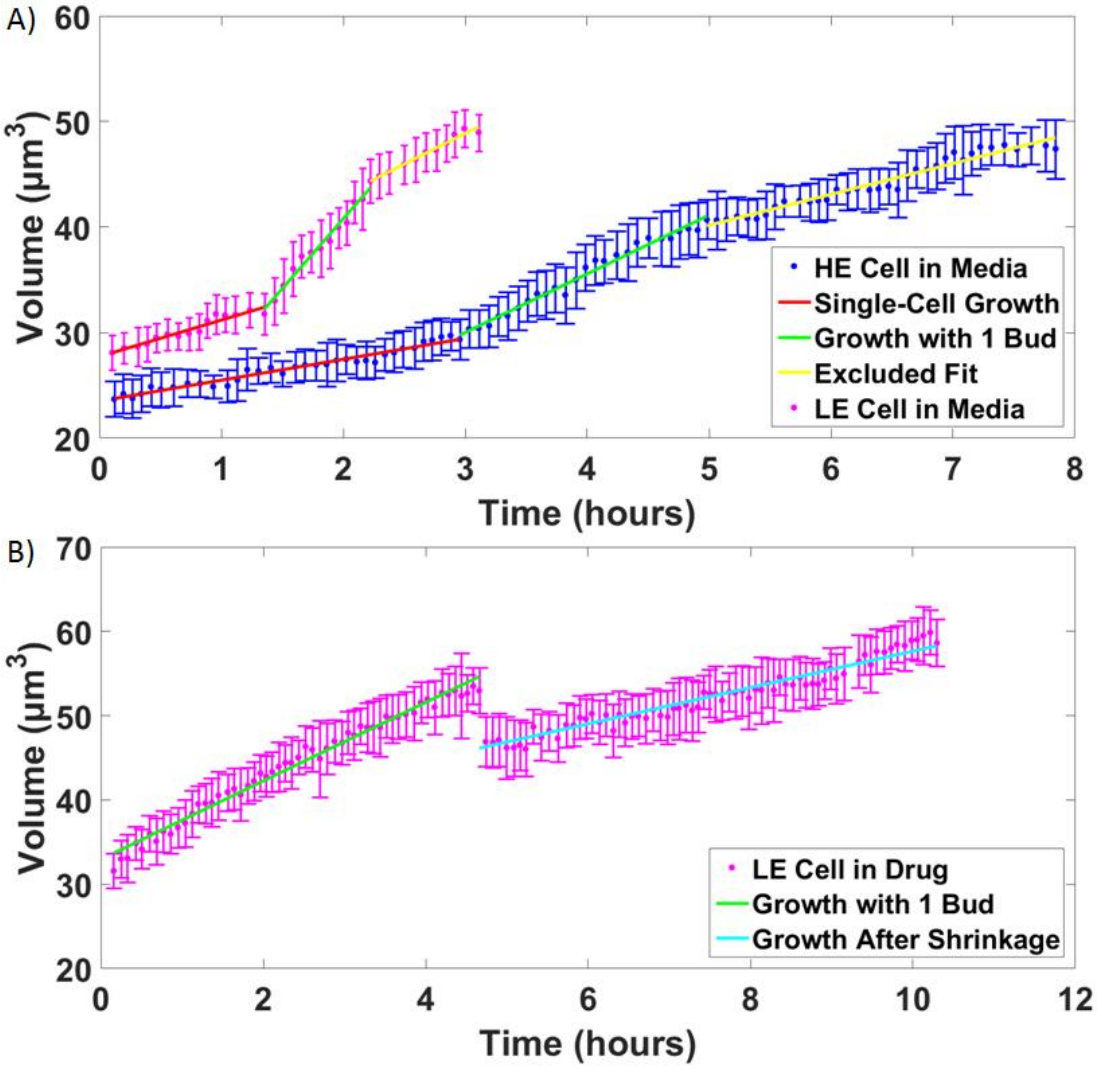

Figure 3.3 Each data point shown here is a ~5 min average where the error bars represent the standard deviation of the raw data points about this average. A) A typical example of observed growth curves and their fits. Curves for LE and HE cells in media are shown in pink and blue respectively. The slope from the linear fit denoted by the red line gives the single-cell growth rate of only a mother cell. The slope from the green line yields the collective growth rate with 1 bud (see Supplementary) and captures the rapid volumetric increase following entry into the S phase of the cell cycle. The negative change in the slope denoted with the yellow line still represents the collective growth of both the mother and one daughter, but it is slower and is not considered for fitness assessment. B) An example of the phenomenon where LE cells in the drugged environment that have produced a bud experience an abrupt drop in the measured volume. Despite the shrinkage of the first daughter, the mother remains alive and there is still continued growth. The slope of the magenta line yields this rate.

Table 1 Averaged data from individual experiments (between 8 and 13 experiments were performed for each of the four conditions, see tables in Supporting Material for details). The uncertainties in the quoted values are the standard errors associated with each computed mean. Reproductive success (yes or no) is characterized by observing at least one successful mitotic division from time-lapsed images. The percentage is with respect to all experiments per condition.

	LE Cells in Regular Media	HE cells in Regular Media	LE Cells in 0.1μg/mL Cycloheximide	HE Cells in 0.1μg/mL Cycloheximide
Mean Single-cell Growth Rate ($x10^{-3}$)	1.5±0.2 μm^3/sec	0.51±0.04 μm^3/sec	0.30±0.05 μm^3/sec	0.52±0.04 μm^3/sec
Mean Collective Growth Rate with 1 Bud ($x10^{-3}$)	4.2±0.3 μm^3/sec	2.0±0.2 μm^3/sec	1.0±0.1 μm^3/sec	1.6±0.1μm^3/sec
Mean Time Between Emergence of 1st and 2nd Daughters	115±3 min	150±17 min	533±50 min	15000±2000 min
Reproductive Success Among All Trials	100%	100%	0%	100%

In comparing the tabulated averages, we see that in the regular media environment, LE cells not only grow faster than the HE cells but also have the highest absolute growth rates and the shortest time between divisions. Thus the LE phenotype has the optimum fitness in this condition. In the toxic environment, we see that the mean single-cell growth rate for HE cells is very similar to the corresponding one in regular media, where (0.52±0.04) $x10^{-3}$ μm^3/sec and (0.51±0.04) $x10^{-3}$ μm^3/sec, respectively, are within their standard errors. The mean collective growth rate with 1 bud is slightly faster for HE cells in regular media than those in cycloheximide. The interdivision time also is noticeably longer for HE cells growing in cycloheximide. Thus, there may be a slight decrease in fitness for HE cells when in the drugged environment. But the LE cells grown in cycloheximide suffer from the worst fitness and the greatest disparity between environments. Not only are the growth rates the lowest amongst all four regimes, they suffer a fivefold drop in the mean single-cell growth rate and experience a shrinking phenomenon unseen amongst the other groups.

The LE cells which began division shortly before or after the start of the experiment, when drugged media was switched into the device, continued to do so for a time, but none

were able to successfully complete reproduction with the first daughter, always leading to a shrinking event. While not shown in Table 1, there was continued growth even after this event, as was denoted in Figure 3.3B. For the cases where this phenomenon was observed, a growth rate following the abrupt drop in measured volume was determined by a linear fit, and the mean of all such values was computed to be (0.6±0.1) $x10^{-3}$ μm^3/sec. It is less than the mean collective growth rate with 1 bud, which represents procession towards mitosis, but greater than the mean single-cell growth rate, which represents the sole growth of the mother cell. There were however three cases where a second daughter was able to emerge near the end of the experiment despite the apparent death of the first, allowing for estimates of the interdivision time. The cells that were not close to division at the beginning of the experiment were greatly inhibited from doing so. While these single cells did continue to grow, they did not attempt to initiate division over an experimental time period of at least 4 times the duration required for reproduction by LE cells in regular media. Therefore, LE cells in cycloheximide either attempted division and failed or were prevented from doing so altogether, resulting in 0% reproductive success over the course of the experiment. These factors only serve to exacerbate the fitness of the LE phenotype in the drugged environment.

3.3 Discussion

We have shown bimodality in the expression of yeast multidrug resistance where the phenotypic heterogeneity indeed leads to differing fitnesses. In favorable growth conditions, the LE subpopulation is better adapted than the HE subpopulation due to faster reproduction, as shown in Figure 3.2A. For LE cells in media, the mean single-cell growth rate is a factor of 3 higher than that for the HE cells while the mean collective growth rate with 1 bud is a factor of 2 higher. However, the rare HE subpopulation's slower growth has reflected its increased resilience to a toxic environment, where it suffers almost no penalty compared to the LE cells. A two-tailed unpaired t-test comparing the mean single-cell growth rates for HE cells in both environments confirmed that there is no statistical difference between the two means, with an overwhelming probability of a true null hypothesis. In looking at the mean collective growth rate with 1 bud in Table 1, it appears that the HE cells dividing in cycloheximide grow slightly slower than in media, but a t-test between these growth rates yielded a t-statistic of 1.726, shy

of exceeding the required 1.753 for a one-tailed α of 0.05. Nonetheless, the presence of cycloheximide could still be having minor detrimental effects on the HE cells. As shown in Table 1, the doubling time is protracted for the HE cells in cycloheximide, and a one-tailed unpaired t-test with α = 0.05 confirms a statistically significant difference in the mean doubling times for HE cells in media versus drug. Coupling this fact with the numeric proximity of the 1.726 t-statistic to the corresponding critical value suggests that there may be an emerging cost for the HE cells at the given level of cycloheximide used.

The concentration of 0.1 μg/mL chosen for the experiments was to ensure an effect but with growth still possible so that fitness could be evaluated. Other studies with budding yeast have used concentrations ranging from one to three orders of magnitude higher[153][154][155], and it has been shown that lower concentrations do not completely inhibit protein synthesis[156]. In fact, a study which used 0.1 μg/mL demonstrated that protein synthesis rates can stabilize at a lower constant value[157]. Therefore it is likely that at this concentration, the effect of cycloheximide is simply small for the HE cells, as the mean single-cell growth rates showed no appreciable difference. But cell cycle phases involving DNA synthesis and mitosis may have shown some more sensitivity due to greater demands in protein translation, which could explain the lengthened amount of time between divisions. Perhaps at higher concentrations, a more statistically significant distinction will arise.

For the LE cells, the fitness disparity between the environments is drastic, with a 5 fold drop in the mean single-cell growth rate and a 4 fold drop in the mean collective growth rate with 1 bud, as shown in Table 1. By performing a one-tailed unpaired t-test comparing the mean single-cell growth rate of the LE cells in drug to those of the HE cells in both environments, we find a significant statistical difference in each case for both α = 0.05 and α = 0.01. This confirms that the growth rate of LE cells in drug is indeed the lowest. Therefore, the relative fitness of the HE cells with respect to the LE cells across these two environments shows a reversal in the better performing phenotype. In addition, the LE cells experience failed attempts at reproduction or complete inhibition from it. Cells in the other three regimes were all able to demonstrate successful advancement through mitosis; LE cells in cycloheximide were

the only ones where 0% of the samples had reproductive success. This further establishes the poor fitness of this phenotype in the drugged environment.

The triggers and mechanisms underlying the shrinking event however remain unclear. Cycloheximide is a broad inhibiter of protein synthesis in eukaryotes, thus it should interfere with all phases of the cell cycle. However, some of the LE cells were able to begin division shortly after introduction of the cycloheximide-dosed media. This implies that despite a toxic presence, they successfully proceeded into S phase. But it is not immediately aborted and is maintained for up to several hours until an abrupt shrinking event that detectably occurs over seconds. Though the effects of cycloheximide could be playing a role in impeding and delaying apoptosis[154], how a necrotic death is prompted only after prolonged exposure is unclear. As for why there is an abrupt drop in the measured volume, at the relatively low driving frequency of 100 kHz, an intact cell membrane contributes are large capacitive impedance[58], but a sudden loss of membrane integrity would result in an increase of ionic current through the volume occupied by the cell and a corresponding decrease in the magnitude of the impedance pulse. This is supported by the fact that necrotic death is characterized by a rapid increase in the permeability of the plasma membrane[158]. However, the growth rate evaluated following the shrinking event is greater than the mean single-cell growth rate of LE cells in drug while being less than their mean collective growth rate before the shrinking occurred. It is understandable that cell contents would leak into the environment given the loss of membrane integrity, but considering the comparison that was just given, it may be possible that the mother was reabsorbing some of the matter in the bud.

The LE cells that did not initiate division at the beginning were not observed to do so throughout the entirety of the experiment. It is most likely that the insufficient number of efflux pumps resulted in a concentration of cycloheximide within the cell that was able to keep it arrested in the G1 phase[156]. The G1 checkpoint can be effectively obstructed by blocking the translation of important proteins for the transition into S phase[159][160]. Although in three cases, a second bud emerged despite the previous death of the first daughter, but their viabilities were undetermined. Since the presence of cycloheximide induces increased PDR5

transcription[152], it was possible that those mother cells were able produce more efflux pumps over time to expel enough cycloheximide and manage a degree of protein synthesis that allowed procession through the G1 checkpoint. However, none of this culminated in confirmed reproductive success over the observation period.

We have therefore demonstrated that in this isogenic strain of budding yeast, each of the two phenotypes conferred a different fitness advantage depending on the environment, true of bet-hedging. Thus by maintaining a small subpopulation of high PDR5 expression cells, the entire population avoids the risk of complete extinction in the event of a sudden shift to a highly toxic environment where greater resistance is needed. However, it is not entirely clear as to why an over-expression of PDR5 leads to slower growth. We know that it produces a transmembrane efflux pump, so this may lead to indiscriminate removal of nutrients or other necessary compounds from within the cytosol. This pump also requires ATP hydrolysis to function, thus an over-abundant number of them would become an onerous energy expenditure for the cell. In fact, a recent study found that in *S. cerevisiae*, excessive expression of proteins containing membrane-protruding regions resulted in a very high fitness cost[161]. Nonetheless, this is consistent with studies that show a slower growth rate is correlated with an increased resilience to stress[151][162][163].

In terms of inheritance, it seems that within at least two generations, the LE and HE states are conserved. While we have not observed phenotypic switching between the states over the course of these experiments, it may yet be revealed if single cells are observed over a much longer period of time and over more generations. The precise control of conditions and the small length scales of microfluidics can be particularly useful for this. And since stochasticity in yeast gene expression is known[164], the inhibition and promotion of PDR5 transcription most likely contain stochastic mechanisms capable of inducing reversible switching between the phenotypes. Hence, this strongly requires further investigation.

3.4 Conclusion

Using a microscopy-integrated microfluidic impedance sensor with on-chip media exchange, we have evaluated the fitness of individual isogenic yeast cells exhibiting bimodal

expression of the PDR5 gene. While the LE cells have the higher fitness in media, severe deficiencies are apparent in the cytotoxic environment. HE cells which possess greater multidrug resistance are able to cope almost equally well in both conditions, becoming the prevailing phenotype under cycloheximide treatment. Therefore, we report a first time observation of bet-hedging in yeast multidrug resistance and indeed in eukaryotic multidrug resistance. We hope the evidence for this evolutionary strategy at work in MDR will lend more insight into gene regulation, the drug response and survivability of pathogenic cells such as those in cancer, and the development of better treatments and therapies.

3.5 Supplementary Tables

In the trials where a single mother cell did not produce a bud during the experiment, began with a bud already, or where the second daughter did not emerge over the course of the experiment, the associated entry in the table is filled with not applicable (NA). Error on each tabulated growth rate is the standard error of the slope coefficient from the linear regression. Errors on the mean values quoted in the captions are the standard errors of the mean computed from the tabulated values in each respective column.

Table B. LE Cells Grown On-chip in Media

Growth Rate of Single Cell x10^{-3} (μm^3/sec)	**Collective Growth Rate with 1 Bud x10^{-3} (μm^3/sec)**	**Time Between Emergence of 1st and 2nd buds (sec)**
2.0±0.1	4.8±0.1	6700±300
1.96±0.06	5.0±0.2	6300±300
1.2±0.1	3.8±0.2	6700±300
1.24±0.09	4.5±0.2	7500±300
1.69±0.04	5.8±0.5	6700±300
0.98±0.06	3.47±0.07	6500±300
1.71±0.07	3.3±0.2	7200±300
1.27±0.03	3.72±0.06	>8400
1.00±0.06	3.5±0.1	7350*
2.4±0.2	4.2±0.2	>5900

The mean growth rates (x10^{-3}) for columns one and two are 1.5±0.2 μm^3/sec and 4.2±0.3 μm^3/sec respectively. The mean doubling time from column three is 6900±200 sec. Lower-bounded times indicate that a second daughter did not emerge before the conclusion of the experiment, though it would have occurred given more time. *For this case, a close estimate of the time is unknown, however the upper and lower bounds are known: 6900 < t < 7800. A mean of these bounds is used.

Table C. HE Cells Grown On-chip in Media

Growth Rate of Single Cell x10^{-3} (μm^3/sec)	Collective Growth Rate with 1 Bud x10^{-3} (μm^3/sec)	Time Between Emergence of 1st and 2nd buds (sec)
NA	1.21±0.04	>10400
0.41±0.01	1.81±0.03	NA
0.55±0.01	1.95±0.06	NA
0.363±0.007	1.60±0.06	9600±300
0.58±0.02	1.63±0.06	8700±300
0.43±0.03	2.53±0.06	7200±300
0.56±0.02	1.78±0.04	16300±300
0.58±0.02	2.23±0.09	8700±300
0.324±0.006	1.37±0.06	10000±300
0.80±0.02	3.43±0.08	7700±300
0.50±0.01	2.09±0.09	7400±300

The mean growth rates (x10^{-3}) for columns one and two are 0.51±0.04 μm^3/sec and 2.0±0.2 μm^3/sec respectively. The mean doubling time from column three is 9000±1000 sec. The two NA entries in this table were due to insufficient imaging data.

Table D. HE Cells Grown On-chip in Cycloheximide

Growth Rate of Single Cell x10^{-3} (μm^3/sec)	Collective Growth Rate with 1 Bud x10^{-3} (μm^3/sec)	Time Between Emergence of 1st and 2nd buds (sec)
0.392±0.006	1.63±0.03	13500±300
0.50±0.03	1.88±0.05	15000±300
0.42±0.01	1.42±0.03	9900±300
0.55±0.01	1.44±0.04	9300±300
NA	1.17±0.04	23700±300
NA	1.42±0.05	26700±300
0.55±0.01	2.01±0.07	9600±300
0.69±0.03	1.84±0.04	9900±300

The mean growth rates (x10^{-3}) for columns one and two are 0.52± 0.04 μm^3/sec and 1.6±0.1 μm^3/sec respectively. The mean doubling time from column three is 15000± 2000sec.

Table E. LE Cells Grown On-chip in Cycloheximide

Growth Rate of Single Cell x10^{-3} (μm^3/sec)	Collective Growth Rate with 1 Bud x10^{-3} (μm^3/sec)	Growth Rate After Shrinkage x10^{-3} (μm^3/sec)	Time Between Emergence of 1st and 2nd buds (sec)
NA	1.40±0.03	0.87±0.04	27000±300
0.558±0.009*	NA	NA	NA
NA	0.83±0.02	0.35±0.07	36600±600
NA	0.862±0.006	0.8±0.2	>50300
NA	0.81±0.02	NA(but occurred)	>28000
NA	1.29±0.02	0.60±0.02	32400±600
0.239±0.002**	NA	NA	NA
NA	0.82±0.03	0.47±0.02	>33000
0.431±0.006*	NA	NA	NA
0.207±0.005***	NA	NA	NA
0.163±0.004***	NA	NA	NA
0.192±0.004***	NA	NA	NA
0.311±0.008***	NA	NA	NA

The mean growth rates (x10^{-3}) for columns one and two are 0.30±0.05 μm^3/sec and 1.0±0.1 μm^3/sec respectively. For the case where shrinking occurred, the mean growth rate (x10^{-3}) from column three is 0.6±0.1 μm^3/sec. The mean doubling time from column four is 32000±3000 sec. Some doubling times are lower-bounded because no second daughter had emerged by the end of the experiment. *No budding was observed for experimental durations of 10 and 11 hours respectively. **No budding was observed for an experimental duration of 21 hours but there was a slope change at ~11.5 hours; the quoted growth rate is an average of the slopes from two linear fits: 0.344±0.002 and 0.134±0.003 (x10^{-3} μm^3/sec). ***No budding was observed for an experimental duration of 9 hours.

Table F. Results for Unpaired T-Tests Between Two Samples with Unequal Variances

Comparison of Interest	Number of Tails	t-statistic	Calculated Degrees of Freedom in Comparison	Critical value for α = 0.05
Single-cell growth rates of HE cells in drug vs. in media	Two-tailed	0.118	13	2.16
Growth rates with 1 bud of HE cells in drug vs. in media	One-tailed	1.726	15	1.753
Doubling times of HE cells in drug vs. in media	One-tailed	1.993	10	1.812
Single-cell growth rates of LE cells in drug vs. those of HE cells in drug	One-tailed	3.089*	11	1.796
Single-cell growth rates of LE cells in drug vs. those of HE cells in media	One-tailed	2.989*	13	1.771

*Also passes t-test for α = 0.01.

4. Conclusion

A microscopy-integrated microfluidic volume sensor capable of measuring the growth rate of single cells was demonstrated in this work. It was then applied to quantitatively evaluate the fitness of two isogenic subpopulations of budding yeast exhibiting different expression levels of the PDR5 gene. The results indicated that the phenotypic heterogeneity of PDR5 expression is bet-hedging, and is also the first known case of bet-hedging in eukaryotic multidrug resistance. Work of this nature is expected to continue as cell growth and fitness are good ways to study the cell cycle and to assess the effects of perturbations on cells, especially with the ability to fluctuate the on-chip environment. For example, the device could be used to monitor the effects of genetic modifications, the dependence of growth on metabolic pathways, the efficacy of cytotoxic drugs, and even the adaptive changes of single cells. But the foundation of impedance sensing can also be appropriated for other purposes, such as cell counting and dielectric spectroscopy. After all, the goal is to provide next-generation biosensors that can tackle life science problems in new and innovative ways. Therefore, the focus of future work can be turned to technological improvements as well.

The greatest source of error for the volume measurement is sensitivity to variations in position and orientation. By implementing position control using acoustic forces or by integrating parallel electrodes, the precision of the measurement can be greatly improved. Another challenge is the throughput of the device. Despite the platform's advantages for single-cell analysis, growth can only be measured for one cell at a time. Thus, parallelization would be vital in circumventing the limits of repeating very long experiments. While these endeavors are not easy, they must still be sought, as impedance cytometry has an important place in the future of both academic research and the development of inexpensive detection devices.

In conclusion, the ability to measure the fitness of single cells has proven very useful and has helped to uncover a new instance of the evolutionary strategy known as bet-hedging. We hope this technology will continue to facilitate research into the intricacies of gene expression and the complexities of cellular growth.

References

[1] deMello AJ. Control and detection of chemical reactions in microfluidic systems. Nature 2006;442:394–402. doi:10.1038/nature05062.

[2] Psaltis D, Quake SR, Yang C. Developing optofluidic technology through the fusion of microfluidics and optics. Nature 2006;442:381–6. doi:10.1038/nature05060.

[3] Craighead H. Future lab-on-a-chip technologies for interrogating individual molecules. Nature 2006;442:387–93. doi:10.1038/nature05061.

[4] El-Ali J, Sorger PK, Jensen KF. Cells on chips. Nature 2006;442:403–11. doi:10.1038/nature05063.

[5] Yager P, Edwards T, Fu E, Helton K, Nelson K, Tam MR, et al. Microfluidic diagnostic technologies for global public health. Nature 2006;442:412–8. doi:10.1038/nature05064.

[6] Squires TM, Quake SR. Microfluidics: Fluid physics at the nanoliter scale. Rev Mod Phys 2005;77:977.

[7] Acheson DJ. Elementary Fluid Dynamics. New York: Clarendon Press; 1990.

[8] Westerhof N, Stergiopulos N, Noble MM. Law of Poiseuille. Snapshots Hemodynamics, Springer US; 2010, p. 9–14.

[9] Segre G, Silberberg A. Behaviour of macroscopic rigid spheres in Poiseuille flow Part 2. Experimental results and interpretation. J Fluid Mech 1962;14:136–57.

[10] Whitesides GM. The origins and the future of microfluidics. Nature 2006;442:368–73. doi:10.1038/nature05058.

[11] Iliescu C, Taylor H, Avram M, Miao J, Franssila S. A practical guide for the fabrication of microfluidic devices using glass and silicon. Biomicrofluidics 2012;6:016505.

[12] Abgrall P, Gué A-M. Lab-on-chip technologies: making a microfluidic network and coupling it into a complete microsystem—a review. J Micromechanics Microengineering 2007;17:R15–49. doi:10.1088/0960-1317/17/5/R01.

[13] Soft lithography. Annu Rev Mater Sci 1998;37:551–75. doi:10.1146/annurev.matsci.28.1.153.

[14] Unger MA, Chou H-P, Thorsen T, Scherer A, Quake SR. Monolithic microfabricated valves and pumps by multilayer soft lithography. Science 2000;288:113–6.

[15] Wiesendanger R. Microfluidic Large-Scale Integration. Science 2000;289:930.

[16] Streets AM, Huang Y. Chip in a lab: Microfluidics for next generation life science research. Biomicrofluidics 2013;7:011302. doi:10.1063/1.4789751.

[17] Manz A, Graber N, Widmer H. Miniaturized total chemical analysis systems: A novel concept for chemical sensing. Sens Actuators B Chem 1990;1:244–8. doi:10.1016/0925-4005(90)80209-I.

[18] Teh S-Y, Lin R, Hung L-H, Lee AP. Droplet microfluidics. Lab Chip 2008;8:198. doi:10.1039/b715524g.

[19] Jebrail MJ, Bartsch MS, Patel KD. Digital microfluidics: a versatile tool for applications in chemistry, biology and medicine. Lab Chip 2012;12:2452. doi:10.1039/c2lc40318h.

[20] Tahvildari R, Beamish E, Tabard-Cossa V, Godin M. Integrating nanopore sensors within microfluidic channel arrays using controlled breakdown. Lab Chip 2015;15:1407–11. doi:10.1039/C4LC01366B.

[21] Lee C-Y, Chang C-L, Wang Y-N, Fu L-M. Microfluidic Mixing: A Review. Int J Mol Sci 2011;12:3263–87. doi:10.3390/ijms12053263.

[22] Luong T-D, Phan V-N, Nguyen N-T. High-throughput micromixers based on acoustic streaming induced by surface acoustic wave. Microfluid Nanofluidics 2011;10:619–25. doi:10.1007/s10404-010-0694-0.

[23] Chen C-K, Cho C-C. Electrokinetically driven flow mixing utilizing chaotic electric fields. Microfluid Nanofluidics 2008;5:785–93. doi:10.1007/s10404-008-0286-4.

[24] Pethig R. Dielectrophoresis: Status of the theory, technology, and applications. Biomicrofluidics 2010;4:022811. doi:10.1063/1.3456626.
[25] Pamme N. Magnetism and microfluidics. Lab Chip 2006;6:24–38. doi:10.1039/B513005K.
[26] Tofteberg T, Skolimowski M, Andreassen E, Geschke O. A novel passive micromixer: lamination in a planar channel system. Microfluid Nanofluidics 2010;8:209–15. doi:10.1007/s10404-009-0456-z.
[27] Stroock AD, Dertinger SK, Ajdari A, Mezić I, Stone HA, Whitesides GM. Chaotic mixer for microchannels. Science 2002;295:647–51.
[28] Wyatt Shields IV C, Reyes CD, López GP. Microfluidic cell sorting: a review of the advances in the separation of cells from debulking to rare cell isolation. Lab Chip 2015;15:1230–49. doi:10.1039/C4LC01246A.
[29] Devendran C, Gralinski I, Neild A. Separation of particles using acoustic streaming and radiation forces in an open microfluidic channel. Microfluid Nanofluidics 2014;17:879–90. doi:10.1007/s10404-014-1380-4.
[30] Franke T, Braunmüller S, Schmid L, Wixforth A, Weitz DA. Surface acoustic wave actuated cell sorting (SAWACS). Lab Chip 2010;10:789. doi:10.1039/b915522h.
[31] Hu X, Bessette PH, Qian J, Meinhart CD, Daugherty PS, Soh HT. Marker-specific sorting of rare cells using dielectrophoresis. Proc Natl Acad Sci U S A 2005;102:15757–61.
[32] Huang Y, Joo S, Duhon M, Heller M, Wallace B, Xu X. Dielectrophoretic Cell Separation and Gene Expression Profiling on Microelectronic Chip Arrays. Anal Chem 2002;74:3362–71. doi:10.1021/ac011273v.
[33] Hoshino K, Huang Y-Y, Lane N, Huebschman M, Uhr JW, Frenkel EP, et al. Microchip-based immunomagnetic detection of circulating tumor cells. Lab Chip 2011;11:3449. doi:10.1039/c1lc20270g.
[34] Jonáš A, Zemánek P. Light at work: The use of optical forces for particle manipulation, sorting, and analysis. ELECTROPHORESIS 2008;29:4813–51. doi:10.1002/elps.200800484.
[35] Karimi A, Yazdi S, Ardekani AM. Hydrodynamic mechanisms of cell and particle trapping in microfluidics. Biomicrofluidics 2013;7:021501. doi:10.1063/1.4799787.
[36] Nieuwstadt HA, Seda R, Li DS, Fowlkes JB, Bull JL. Microfluidic particle sorting utilizing inertial lift force. Biomed Microdevices 2011;13:97–105. doi:10.1007/s10544-010-9474-6.
[37] Zare RN, Kim S. Microfluidic Platforms for Single-Cell Analysis. Annu Rev Biomed Eng 2010;12:187–201. doi:10.1146/annurev-bioeng-070909-105238.
[38] Wheeler AR, Throndset WR, Whelan RJ, Leach AM, Zare RN, Liao YH, et al. Microfluidic Device for Single-Cell Analysis. Anal Chem 2003;75:3581–6. doi:10.1021/ac0340758.
[39] McClain MA, Culbertson CT, Jacobson SC, Allbritton NL, Sims CE, Ramsey JM. Microfluidic Devices for the High-Throughput Chemical Analysis of Cells. Anal Chem 2003;75:5646–55. doi:10.1021/ac0346510.
[40] Zheng Y, Nguyen J, Wei Y, Sun Y. Recent advances in microfluidic techniques for single-cell biophysical characterization. Lab Chip 2013;13:2464. doi:10.1039/c3lc50355k.
[41] Pajerowski JD, Dahl KN, Zhong FL, Sammak PJ, Discher DE. Physical plasticity of the nucleus in stem cell differentiation. Proc Natl Acad Sci 2007;104:15619–24.
[42] Di Carlo D. A mechanical biomarker of cell state in medicine. J Lab Autom 2012;17:32–42.
[43] Nishino M, Tanaka H, Ogura H, Inoue Y, Koh T, Fujita K, et al. Serial Changes in Leukocyte Deformability and Whole Blood Rheology in Patients With Sepsis or Trauma: J Trauma Inj Infect Crit Care 2005;59:1425–31. doi:10.1097/01.ta.0000197356.83144.72.
[44] Dulińska I, Targosz M, Strojny W, Lekka M, Czuba P, Balwierz W, et al. Stiffness of normal and pathological erythrocytes studied by means of atomic force microscopy. J Biochem Biophys Methods 2006;66:1–11. doi:10.1016/j.jbbm.2005.11.003.

[45] Suresh S. Nanomedicine: Elastic clues in cancer detection. Nat Nano 2007;2:748–9. doi:10.1038/nnano.2007.397.
[46] Rosenbluth MJ, Lam WA, Fletcher DA. Analyzing cell mechanics in hematologic diseases with microfluidic biophysical flow cytometry. Lab Chip 2008;8:1062. doi:10.1039/b802931h.
[47] Hou HW, Li QS, Lee GYH, Kumar AP, Ong CN, Lim CT. Deformability study of breast cancer cells using microfluidics. Biomed Microdevices 2009;11:557–64. doi:10.1007/s10544-008-9262-8.
[48] Lee SS, Yim Y, Ahn KH, Lee SJ. Extensional flow-based assessment of red blood cell deformability using hyperbolic converging microchannel. Biomed Microdevices 2009;11:1021–7. doi:10.1007/s10544-009-9319-3.
[49] Gossett DR, Henry TK, Lee SA, Ying Y, Lindgren AG, Yang OO, et al. Hydrodynamic stretching of single cells for large population mechanical phenotyping. Proc Natl Acad Sci 2012;109:7630–5.
[50] Godin M, Delgado FF, Son S, Grover WH, Bryan AK, Tzur A, et al. Using buoyant mass to measure the growth of single cells. Nat Methods 2010;7:387–90. doi:10.1038/nmeth.1452.
[51] Bryan AK, Hecht VC, Shen W, Payer K, Grover WH, Manalis SR. Measuring single cell mass, volume, and density with dual suspended microchannel resonators. Lab Chip 2014;14:569–76. doi:10.1039/C3LC51022K.
[52] Nilsson J, Evander M, Hammarström B, Laurell T. Review of cell and particle trapping in microfluidic systems. Anal Chim Acta 2009;649:141–57. doi:10.1016/j.aca.2009.07.017.
[53] Gossett DR, Weaver WM, Mach AJ, Hur SC, Tse HTK, Lee W, et al. Label-free cell separation and sorting in microfluidic systems. Anal Bioanal Chem 2010;397:3249–67. doi:10.1007/s00216-010-3721-9.
[54] Lo YJ, Lei U, Chen KY, Lin YY, Huang CC, Wu MS, et al. Derivation of the cell dielectric properties based on Clausius-Mossotti factor. Appl Phys Lett 2014;104:113702. doi:10.1063/1.4869480.
[55] Sun T, Morgan H. Single-cell microfluidic impedance cytometry: a review. Microfluid Nanofluidics 2010;8:423–43. doi:10.1007/s10404-010-0580-9.
[56] Coulter WH. Means for counting particles suspended in a fluid. US2656508, 1953.
[57] Tzur A, Moore JK, Jorgensen P, Shapiro HM, Kirschner MW. Optimizing Optical Flow Cytometry for Cell Volume-Based Sorting and Analysis. PLoS ONE 2011;6:e16053. doi:10.1371/journal.pone.0016053.
[58] Morgan H, Sun T, Holmes D, Gawad S, Green NG. Single cell dielectric spectroscopy. J Phys Appl Phys 2007;40:61–70. doi:10.1088/0022-3727/40/1/S10.
[59] Zheng Y, Shojaei-Baghini E, Azad A, Wang C, Sun Y. High-throughput biophysical measurement of human red blood cells. Lab Chip 2012;12:2560. doi:10.1039/c2lc21210b.
[60] Chen J, Zheng Y, Tan Q, Shojaei-Baghini E, Zhang YL, Li J, et al. Classification of cell types using a microfluidic device for mechanical and electrical measurement on single cells. Lab Chip 2011;11:3174. doi:10.1039/c1lc20473d.
[61] Gawad S, Schild L, Renaud P. Micromachined impedance spectroscopy flow cytometer for cell analysis and particle sizing. Lab Chip 2001;1:76. doi:10.1039/b103933b.
[62] Mei Z, Cho SH, Zhang A, Dai J, Wu T-F, Lo Y-H. Counting leukocytes from whole blood using a lab-on-a-chip Coulter counter. Eng. Med. Biol. Soc. EMBC 2012 Annu. Int. Conf. IEEE, IEEE; 2012, p. 6277–80.
[63] Delgado AV, González-Caballero F, Hunter RJ, Koopal LK, Lyklema J. Measurement and Interpretation of Electrokinetic Phenomena (IUPAC Technical Report). Pure Appl Chem 2005;77. doi:10.1351/pac200577101753.
[64] Katsumoto Y, Tatsumi K, Doi T, Nakabe K. Electrical classification of single red blood cell deformability in high-shear microchannel flows. Int J Heat Fluid Flow 2010;31:985–95. doi:10.1016/j.ijheatfluidflow.2010.02.019.

[65] Schwan HP. Electrode polarization impedance and measurements in biological materials*. Ann N Y Acad Sci 1968;148:191–209.
[66] Ayliffe HE, Rabbitt RD, others. Electric impedance spectroscopy using microchannels with integrated metal electrodes. Microelectromechanical Syst J Of 1999;8:50–7.
[67] Kuang W, Nelson SO. Low-frequency dielectric properties of biological tissues: a review with some new insights. Trans ASAE-Am Soc Agric Eng 1998;41:173–84.
[68] Schwan HP. Electrical properties of tissues and cell suspensions: mechanisms and models. Eng. Med. Biol. Soc. 1994 Eng. Adv. New Oppor. Biomed. Eng. Proc. 16th Annu. Int. Conf. IEEE, IEEE; 1994, p. A70–1.
[69] Sillars RW. The properties of a dielectric containing semiconducting particles of various shapes. Inst Electr Eng - Proc Wirel Sect Inst 1937;12:139–55(16).
[70] Cima I, Wen Yee C, Iliescu FS, Min Phyo W, Hon Lim K, Iliescu C, et al. Label-free isolation of circulating tumor cells in microfluidic devices: Current research and perspectives. Biomicrofluidics 2013;7:011810. doi:10.1063/1.4780062.
[71] Kozak D, Broom M, Vogel R. High Resolution Particle Characterization to Expedite Development and Regulatory Acceptance of Nanomedicines. Curr Drug Deliv 2015;12:115–20.
[72] Ona T, Shibata J. Advanced dynamic monitoring of cellular status using label-free and non-invasive cell-based sensing technology for the prediction of anticancer drug efficacy. Anal Bioanal Chem 2010;398:2505–33. doi:10.1007/s00216-010-4223-5.
[73] Mitchison JM. Growth during the cell cycle. Int Rev Cytol 2003;226:165–258.
[74] Wang JD, Levin PA. Metabolism, cell growth and the bacterial cell cycle. Nat Rev Microbiol 2009;7:822–7.
[75] Botstein D, Chervitz SA, Cherry JM. Yeast as a model organism. Sci N Y NY 1997;277:1259.
[76] Autret S, Levine A, Holland IB, Séror SJ. Cell cycle checkpoints in bacteria. Biochimie 1997;79:549–54. doi:10.1016/S0300-9084(97)82002-0.
[77] Elledge SJ. Cell Cycle Checkpoints: Preventing an Identity Crisis. Science 1996;274:1664–72. doi:10.1126/science.274.5293.1664.
[78] Hartwell, Weinert LH, Ted A. Checkpoints: Controls that Ensure the Order of Cell Cycle Events. Science 1989;246. doi:10.1126/science.2683079.
[79] Hartwell L, Kastan M. Cell cycle control and cancer. Science 1994;266:1821–8. doi:10.1126/science.7997877.
[80] Kumar V, Abbas AK, Fausto N, Aster JC. Robbins & Cotran Pathologic Basis of Disease. Elsevier Health Sciences; 2009.
[81] Sveiczer A, Novak B, Mitchison JM. Size control in growing yeast and mammalian cells. Theor Biol Med Model 2004;1:12–12. doi:10.1186/1742-4682-1-12.
[82] Son S, Tzur A, Weng Y, Jorgensen P, Kim J, Kirschner MW, et al. Direct observation of mammalian cell growth and size regulation. Nat Methods 2012;9:910–2. doi:10.1038/nmeth.2133.
[83] Boye E, Nordström K. Coupling the cell cycle to cell growth: A look at the parameters that regulate cell-cycle events. EMBO Rep 2003;4:757–60. doi:10.1038/sj.embor.embor895.
[84] Brauer MJ, Huttenhower C, Airoldi EM, Rosenstein R, Matese JC, Gresham D, et al. Coordination of growth rate, cell cycle, stress response, and metabolic activity in yeast. Mol Biol Cell 2008;19:352–67.
[85] Yang J, Dungrawala H, Hua H, Manukyan A, Abraham L, Lane W, et al. Cell size and growth rate are major determinants of replicative lifespan. Cell Cycle 2011;10:144–55. doi:10.4161/cc.10.1.14455.
[86] Amir A. Cell Size Regulation in Bacteria. Phys Rev Lett 2014;112. doi:10.1103/PhysRevLett.112.208102.
[87] Qu Z. Coordination of cell growth and cell division: a mathematical modeling study. J Cell Sci 2004;117:4199–207. doi:10.1242/jcs.01294.

[88] Scott M, Gunderson CW, Mateescu EM, Zhang Z, Hwa T. Interdependence of Cell Growth and Gene Expression: Origins and Consequences. Science 2010;330:1099–102. doi:10.1126/science.1192588.
[89] Maitra A, Dill KA. Bacterial growth laws reflect the evolutionary importance of energy efficiency. Proc Natl Acad Sci 2015;112:406–11. doi:10.1073/pnas.1421138111.
[90] Folkman J, Moscona A. Role of cell shape in growth control. Nature 1978;273:345–9. doi:10.1038/273345a0.
[91] Amir A, van Teeffelen S. Getting into shape: How do rod-like bacteria control their geometry? Syst Synth Biol 2014;8:227–35. doi:10.1007/s11693-014-9143-9.
[92] Gillespie JH. Population genetics: a concise guide. Baltimore, Md: The Johns Hopkins University Press; 1998.
[93] Orr HA. The genetic theory of adaptation: a brief history. Nat Rev Genet 2005;6:119–27. doi:10.1038/nrg1523.
[94] Orr HA. Fitness and its role in evolutionary genetics. Nat Rev Genet 2009;10:531–9. doi:10.1038/nrg2603.
[95] Melbinger A, Vergassola M. The Impact of Environmental Fluctuations on Evolutionary Fitness Functions. Sci Rep 2015;5:15211. doi:10.1038/srep15211.
[96] Razinkov IA, Baumgartner BL, Bennett MR, Tsimring LS, Hasty J. Measuring Competitive Fitness in Dynamic Environments. J Phys Chem B 2013;117:13175–81. doi:10.1021/jp403162v.
[97] Kitano H. Systems biology: a brief overview. Science 2002;295:1662–4.
[98] van der Heyden FHJ, Stein D, Dekker C. Streaming Currents in a Single Nanofluidic Channel. Phys Rev Lett 2005;95. doi:10.1103/PhysRevLett.95.116104.
[99] Riordon J, Nash M, Jing W, Godin M. Quantifying the volume of single cells continuously using a microfluidic pressure-driven trap with media exchange. Biomicrofluidics 2014;8:011101. doi:10.1063/1.4867035.
[100] Baldwin WW, Kubitschek HE. Buoyant density variation during the cell cycle of Saccharomyces cerevisiae. J Bacteriol 1984;158:701–4.
[101] Riordon J, Mirzaei M, Godin M. Microfluidic cell volume sensor with tunable sensitivity. Lab Chip 2012;12:3016. doi:10.1039/c2lc40357a.
[102] Riordon J, M.-Catafard N, Godin M. Using the fringing electric field in microfluidic volume sensors to enhance sensitivity and accuracy. Appl Phys Lett 2012;101:154105. doi:10.1063/1.4759033.
[103] Gawad S, Cheung K, Seger U, Bertsch A, Renaud P. Dielectric spectroscopy in a micromachined flow cytometer: theoretical and practical considerations. Lab Chip 2004;4:241. doi:10.1039/b313761a.
[104] Anderson JR, Chiu DT, Wu H, Schueller OJ, Whitesides GM. Fabrication of microfluidic systems in poly (dimethylsiloxane). Electrophoresis 2000;21:27–40.
[105] Lee JN, Park C, Whitesides GM. Solvent Compatibility of Poly(dimethylsiloxane)-Based Microfluidic Devices. Anal Chem 2003;75:6544–54. doi:10.1021/ac0346712.
[106] Regehr KJ, Domenech M, Koepsel JT, Carver KC, Ellison-Zelski SJ, Murphy WL, et al. Biological implications of polydimethylsiloxane-based microfluidic cell culture. Lab Chip 2009;9:2132. doi:10.1039/b903043c.
[107] Benjamin P, Weaver C. The Adhesion of Evaporated Metal Films on Glass. Proc R Soc Lond Math Phys Eng Sci 1961;261:516–31. doi:10.1098/rspa.1961.0093.
[108] Fischer LM, Tenje M, Heiskanen AR, Masuda N, Castillo J, Bentien A, et al. Gold cleaning methods for electrochemical detection applications. Microelectron Eng 2009;86:1282–5. doi:10.1016/j.mee.2008.11.045.
[109] Riordon J. Developing microfluidic volume sensors for cell sorting and cell growth monitoring. PhD Thesis. University of Ottawa, 2014.
[110] Henderson D, Lamperski S. Simple Description of the Capacitance of the Double Layer of a High Concentration Electrolyte. J Chem Eng Data 2011;56:1204–8. doi:10.1021/je101106z.

[111] Wright MR. An Introduction to Aqueous Electrolyte Solutions. Wiley; 2007.
[112] Schwan HP. Alternating current electrode polarization. Biophysik 1966;3:181–201.
[113] Dini JW. Electrodeposition: The Materials Science of Coatings and Substrates. Noyes Publications; 1993.
[114] Feltham AM, Spiro M. Platinized platinum electrodes. Chem Rev 1971;71:177–93.
[115] Zheng S, Liu M, Tai Y-C. Micro coulter counters with platinum black electroplated electrodes for human blood cell sensing. Biomed Microdevices 2008;10:221–31. doi:10.1007/s10544-007-9128-5.
[116] Bernabini C, Holmes D, Morgan H. Micro-impedance cytometry for detection and analysis of micron-sized particles and bacteria. Lab Chip 2011;11:407–12. doi:10.1039/C0LC00099J.
[117] Sun T, Green NG, Gawad S, Morgan H. Analytical electric field and sensitivity analysis for two microfluidic impedance cytometer designs. IET Nanobiotechnol 2007;1:69. doi:10.1049/iet-nbt:20070019.
[118] Li S, Li M, Hui YS, Cao W, Li W, Wen W. A novel method to construct 3D electrodes at the sidewall of microfluidic channel. Microfluid Nanofluidics 2013;14:499–508. doi:10.1007/s10404-012-1068-6.
[119] Choi J-W, Rosset S, Niklaus M, Adleman JR, Shea H, Psaltis D. 3-dimensional electrode patterning within a microfluidic channel using metal ion implantation. Lab Chip 2010;10:783. doi:10.1039/b917719a.
[120] Kadilak AL, Liu Y, Shrestha S, Bernard JR, Mustain WE, Shor LM. Selective deposition of chemically-bonded gold electrodes onto PDMS microchannel side walls. J Electroanal Chem 2014;727:141–7. doi:10.1016/j.jelechem.2014.06.006.
[121] Grenvall C, Antfolk C, Bisgaard CZ, Laurell T. Two-dimensional acoustic particle focusing enables sheathless chip Coulter counter with planar electrode configuration. Lab Chip 2014;14:4629–37. doi:10.1039/C4LC00982G.
[122] Rayleigh, Lord. On Waves Propagated along the Plane Surface of an Elastic Solid. Proc Lond Math Soc 1885;s1-17:4–11.
[123] Yosioka K, Kawasima Y. Acoustic radiation pressure on a compressible sphere. Acta Acust United Acust 1955;5:167–73.
[124] Ding X, Li P, Lin S-CS, Stratton ZS, Nama N, Guo F, et al. Surface acoustic wave microfluidics. Lab Chip 2013;13:3626. doi:10.1039/c3lc50361e.
[125] Shi J, Mao X, Ahmed D, Colletti A, Huang TJ. Focusing microparticles in a microfluidic channel with standing surface acoustic waves (SSAW). Lab Chip 2008;8:221–3. doi:10.1039/B716321E.
[126] Azizi A. Bet hedging in Pdr5-mediated drug resistance and a mechanism for its regulation. M.Sc. Thesis. University of Ottawa, 2014.
[127] Watanabe T. Infective heredity of multiple drug resistance in bacteria. Bacteriol Rev 1963;27:87.
[128] Nikaido H. Multidrug Resistance in Bacteria. Annu Rev Biochem 2009;78:119–46. doi:10.1146/annurev.biochem.78.082907.145923.
[129] Barriere SL. Clinical, economic and societal impact of antibiotic resistance. Expert Opin Pharmacother 2015;16:151–3. doi:10.1517/14656566.2015.983077.
[130] Nathan C. Antibiotics at the crossroads. Nature 2004;431:899–902.
[131] Gulshan K, Moye-Rowley WS. Multidrug Resistance in Fungi. Eukaryot Cell 2007;6:1933–42. doi:10.1128/EC.00254-07.
[132] Longley D, Johnston P. Molecular mechanisms of drug resistance. J Pathol 2005;205:275–92. doi:10.1002/path.1706.
[133] Holohan C, Van Schaeybroeck S, Longley DB, Johnston PG. Cancer drug resistance: an evolving paradigm. Nat Rev Cancer 2013;13:714–26. doi:10.1038/nrc3599.
[134] Gottesman MM, Fojo T, Bates SE. Multidrug Resistance in Cancer: Role of ATP-Dependent Transporters. Nat Rev Cancer 2002;2:48–58. doi:10.1038/nrc706.

[135] Persidis, A. Cancer multidrug resistance. Nat Biotechnol 1999;17:94–5. doi:10.1038/80051.
[136] Shervington A, Lu C. Expression of Multidrug Resistance Genes in Normal and Cancer Stem Cells. Cancer Invest 2008;26:535–42. doi:10.1080/07357900801904140.
[137] Donnenberg VS, Donnenberg AD. Multiple Drug Resistance in Cancer Revisited: The Cancer Stem Cell Hypothesis. J Clin Pharmacol 2005;45:872–7. doi:10.1177/0091270005276905.
[138] Higgins CF. The ABC of channel regulation. Cell 1995;82:693–6.
[139] Jones PM, George AM. The ABC transporter structure and mechanism: perspectives on recent research. Cell Mol Life Sci CMLS 2004;61:682–99. doi:10.1007/s00018-003-3336-9.
[140] Davidson AL, Dassa E, Orelle C, Chen J. Structure, Function, and Evolution of Bacterial ATP-Binding Cassette Systems. Microbiol Mol Biol Rev 2008;72:317–64. doi:10.1128/MMBR.00031-07.
[141] Juliano RL, Ling V. A surface glycoprotein modulating drug permeability in Chinese hamster ovary cell mutants. Biochim Biophys Acta 1976;455:152–62. doi:10.1016/0005-2736(76)90160-7.
[142] Choi C-H. ABC transporters as multidrug resistance mechanisms and the development of chemosensitizers for their reversal. Cancer Cell Int 2005;5:30.
[143] Balzi E, Wang M, Leterme S, Van Dyck L, Goffeau A. PDR5, a novel yeast multidrug resistance conferring transporter controlled by the transcription regulator PDR1. J Biol Chem 1994;269:2206–14.
[144] Balzi E, Goffeau A. Yeast multidrug resistance: the PDR network. J Bioenerg Biomembr 1995;27:71–6.
[145] Wolfger H, Mahé Y, Parle-McDermott A, Delahodde A, Kuchler K. The yeast ATP binding cassette (ABC) protein genes PDR10 and PDR15 are novel targets for the Pdr1 and Pdr3 transcriptional regulators. FEBS Lett 1997;418:269–74.
[146] Lewis K. Persister Cells. Annu Rev Microbiol 2010;64:357–72. doi:10.1146/annurev.micro.112408.134306.
[147] Balaban NQ, Merrin J, Chait R, Kowalik L, Leibler S. Bacterial Persistence as a Phenotypic Switch. Science 2004;305:1622–5. doi:10.1126/science.1099390.
[148] Ripa J, Olofsson H, Jonzen N. What is bet-hedging, really? Proc R Soc B Biol Sci 2010;277:1153–4. doi:10.1098/rspb.2009.2023.
[149] Grimbergen AJ, Siebring J, Solopova A, Kuipers OP. Microbial bet-hedging: the power of being different. Curr Opin Microbiol 2015;25:67–72. doi:10.1016/j.mib.2015.04.008.
[150] de Jong IG, Haccou P, Kuipers OP. Bet hedging or not? A guide to proper classification of microbial survival strategies. BioEssays 2011;33:215–23. doi:10.1002/bies.201000127.
[151] Levy SF, Merrin, Jack, Chait, Remy, Kowalik, Lukasz, Leibler, Stanislas. Bet Hedging in Yeast by Heterogeneous, Age-Correlated Expression of a Stress Protectant. PLoS Biol 2012;10:e1001325. doi:10.1371/journal.pbio.1001325.
[152] Thakur JK, Arthanari H, Yang F, Pan S-J, Fan X, Breger J, et al. A nuclear receptor-like pathway regulating multidrug resistance in fungi. Nature 2008;452:604–9. doi:10.1038/nature06836.
[153] Tran JR, Brodsky JL. Assays to Measure ER-Associated Degradation in Yeast. Methods Mol Biol 2012;832:505–18.
[154] Madeo F, Fröhlich E, Ligr M, Grey M, Sigrist SJ, Wolf DH, et al. Oxygen Stress: A Regulator of Apoptosis in Yeast. J Cell Biol 1999;145:757–67.
[155] Gerlinger U-M, Gückel R, Hoffmann M, Wolf DH, Hilt W. Yeast cycloheximide-resistant crl mutants are proteasome mutants defective in protein degradation. Mol Biol Cell 1997;8:2487–99.
[156] Shilo, B., Riddle, V. G. H., Pardee, A. B. Protein Turnover and Cell-cycle Initiation in Yeast. Exp Cell Res 1979;123:221–7.
[157] Popolo L, Vanoni M, Alberghina L. Control of the yeast cell cycle by protein synthesis. Exp Cell Res 1982;142:69–78. doi:10.1016/0014-4827(82)90410-4.

[158] Proskuryakov SY., Konoplyannikov AG, Gabai VL. Necrosis: a specific form of programmed cell death? Exp Cell Res 2003;283:1–16. doi:10.1016/S0014-4827(02)00027-7.
[159] Balogun FO, Truman AW, Kron SJ. DNA resection proteins Sgs1 and Exo1 are required for G1 checkpoint activation in budding yeast. DNA Repair 2013;12:751–60. doi:10.1016/j.dnarep.2013.06.003.
[160] Skotheim JM, Di Talia S, Siggia ED, Cross FR. Positive feedback of G1 cyclins ensures coherent cell cycle entry. Nature 2008;454:291–6. doi:10.1038/nature07118.
[161] Tomala K, Korona R. Evaluating the Fitness Cost of Protein Expression in Saccharomyces cerevisiae. Genome Biol Evol 2013;5:2051–60. doi:10.1093/gbe/evt154.
[162] Brauer MJ, Huttenhower C, Airoldi EM, Rosenstein R, Matese JC, Gresham D, et al. Coordination of growth rate, cell cycle, stress response, and metabolic activity in yeast. Mol Biol Cell 2008;19:352–67.
[163] Lu C, Brauer MJ, Botstein D. Slow growth induces heat-shock resistance in normal and respiratory-deficient yeast. Mol Biol Cell 2009;20:891–903.
[164] Raser JM, O'Shea EK. Control of stochasticity in eukaryotic gene expression. Science 2004;304:1811–4.

Appendix

AZ Channel Master

Dummy Layer

1. Dry wafer under nitrogen stream and bake for 10 min at 200C (If piranha cleaned. Otherwise skip steps 1 and 2)
2. Cool down for 5 min
3. Set spin coater to following:
   i. 10s @ 500rpm ACL: 100rpm/s
   ii. 60s @ 3000rpm ACL: 500rpm/s
   iii. 10s @ 0 rpm ACL: 300rpm/s
4. Pour SU-8 10 on the wafer ant rotate wafer to allow SU-8 10 fully cover the wafer surface (make sure no defect)
5. Run spinner
6. Carefully remove wafer from spinner ensuring no drips fall on the wafer surface as the lid opens
   i. Ensure the photo resist layer quality is satisfactory. It is a bonding layer so perfection is not necessary as long as the layer is smooth and complete
   ii. If the layer quality is not satisfactory put it back in the spinner and clean with acetone and IPA. Dry and go back to 4
7. Prebake for 2 min @ 75C, then 5 min @ 105C
   i. After 1.5 min up the temperature, set timer for 5.5 min to ensure that wafer is temp for at least 4.5 min
8. Allow baked wafer to cool for 5 min
9. Blank exposure for 20 seconds
10. Post bake for 1 min @ 75 C and 2 min @ 105
    i. After 30s up the temperature, set the timer to 2.5 min to ensure safer is at temperature for at least 1.5 min
11. Develop for 2 min, IPA (isopropanol) rinse

Channel Layer (Target height of sensing channel is 20um)

12. Set spin coater to the following:
    i. 5s @ 300 rpm ACL=100
    ii. 60s @ 1800 rpm ACL=600
    iii. 10s @ 500 rpm ACL =400
    iv. 10s @1000 rpm ACL =250
    v. 5s @ 0 rpm ACL =200
13. Pour on AZ 4620 and rotate wafer to coat entire surface (non-viscous)
14. Run spinner

15. Remove wafer and make sure no drips on surface
    i. Ensure the photo resist layer quality is satisfactory. It is a bonding layer so perfection is not necessary as long as the layer is smooth and complete
    ii. If the layer quality is not satisfactory put it back in the spinner and clean with acetone and IPA. Dry and go back to 13
16. Bake for 85s @110C
17. Let cool for 5 minutes. Pour on AZ 4620 rotate wafer to coat entire surface
18. Set spinner:
    i. 5s @ 300 rpm ACL=100
    ii. 60s @ 1000 rpm ACL=200
    iii. 10s @ 500 rpm ACL=200
    iv. 10s @ 1000rpm ACL=250
    v. 5s @ 0 rpm ACL = 200
19. Run spinner
20. Remove wafer from the spinner and ensure no drips on wafer surface
    i. Ensure the photo resist layer quality is satisfactory. It is a bonding layer so perfection is not necessary as long as the layer is smooth and complete
    ii. If the layer quality is not satisfactory put it back in the spinner and clean with acetone and IPA. Dry and go back to 17
21. Bake for 165s @ 110C
22. Let cool for 5mins.
23. Wait 1 hour to 2 hours (during which SU 8 valve layer can be made) to rehydrate the AZ layer. Tear a white wipe into strips and wet them. Place them around the wafer inside petri dish and cover. Do not let the strips touch the wafer.
24. Expose for 60s. Time may vary depending on bulb intensity adjustments. Can try 45 seconds if too long, or vary at your own discretion.
25. Develop for 5 min in AZ developer. Prepare two dishes, pour AZ developer into both. Place the wafer into the first dish for 1.5min and then move it to the second dish. Constantly agitate. Quickly empty the first dish and replace the developer. At 3 min put the wafer into the other dish. If you notice that all the exposed AZ has been removed, take it out (No need for full 5mins).
26. Rinse with DI water and blow dry (if residue exist, do a quick submersion in developer)
27. Reflow: bake for 5 min each at 75C and 105C or 75C, 105C, and 135C for greater height drops. Wait until 30s is left in the current time interval and then up the temperature, i.e. increase from 75C to 105C at 4.5min, or from 105C to 135C at 9.5min.
28. Check heights and widths with Dektak. If height is much lower, might be the bottle of AZ that's an issue. Order more if results are not consistent, even if the expiration date hasn't been reached. The photoresist is known to be more difficult to work with than SU-8.
29. Lastly, higher channel height can be done using 3 layers of AZ. Can repeat the spin coater conditions for the second layer. Only the speed in step ii) needs to be altered. The third layer's bake should be for 240s @ 110C.

SU-8 Valve Master

1. Blow dry cleaned wafer and back for 10 minutes at 200C to remove water (If piranha cleaned. Otherwise skip steps 1 and 2).
2. Let dry for 5mins.
3. Heat up a hotplate to 65C beforehand.
4. Can use SU-8 10 dummy layer (same procedure as for the channel layer), or just proceed straight to step 4 if wafer is in good condition and photoresist sticks well.
5. Set spin coater to following:
   i. 10s @ 500rpm ACL: 100rpm/s
   ii. 60s @ 3000rpm ACL: 500rpm/s
   iii. 10s @ 0 rpm ACL: 300rpm/s
6. Pour SU-2050 on wafer and rotate for a good coverage, then place on it on the spin coater, center it, and apply vacuum. This will be for ~50µm tall features.
7. Run spin coater.
8. Place wafer on 65C hot plate and immediately dial up to 95C. Set timer for 7mins. Ideally, wafer is at ~65C for 30sec and 95C for at least 6min.
9. Let cool for 5min.
10. Make sure one hotplate is ready at 65C again.
11. Expose 12 sec (adjust as necessary and mind changes to lamp intensity).
12. Take exposed wafer and place on 65C hotplate. Set timer for 6.5 minutes. After 30 seconds, dial up to 95C. Ideally, wafer is at 65C for 1 min and 95C for 5.5 min.
13. Let cool for 5min.
14. SU-8 development for 5 min, then rinse with IPA at the end and blow dry with N2 gun.

Device Fabrication

NOTE:

Before using Valve and Channel Masters, treat them with **aminosilane**, or full name: (tridecafluoro-1,1,2,2-tetrahydrooctyl)trichlorosilane. Place a wafer into vacuum chamber and tear off a piece of those plastic weighing boats and place that inside chamber as well. Pipette a 1 µL drop of the aminosilane onto the torn piece of the weighing boat. Apply vacuum for 5mins. Then stop the vacuum but do not open the t-junction valve. Allow wafer to sit inside vacuumed environment for 1 hour before allowing air back in.

Channel Layer

1. Prepare PDMS in a ratio of 1:20, curing agent to base. Aim for ~11 grams of total mass.
2. Mix for 5-6 minutes.
3. Vacuum for ~1 hour.
4. Bring the AZ channel master and the weighing boat with the PDMS into the clean room
5. Set spin coater to following:
   i. 10s @ 500rpm ACL: 100rpm/s
   ii. 33s @ 2000rpm ACL: 500rpm/s
   iii. 10s @ 0 rpm ACL: 200rpm/s
6. Blow wafer with N2 gun to get rid of any dust and center the wafer on spin coater
7. Pour the PDMS carefully, so as to not create air bubbles. Do it slowly and try to cover as much of the surface around the center of the wafer as possible.
8. Spin, and then remove the wafer and place it into a petri dish.
9. You will notice streaks radiating outward, seen as the light reflects off the PDMS. These will disappear as the PDMS relaxes.
10. Allow the relaxation to occur by using this time to clean up the spin coater.
11. Bring the dish out and bake in oven for 20min at 80C.

Valve Layer

1. Tape the wafer to a circular acrylic frame. Place both into the large petri dish. This will create a well around the wafer for the PDMS to be poured into. Acrylic frame is not necessary if a dish can be found that is around the same diameter as the wafer. Wafer still needs to be taped down, however.
2. Prepare PDMS in a ratio of 1:7, curing agent to base. Depending on the petri dish, the final mass will vary. After the initial cast, you will most likely only need to cut out half of the PDMS that filled up the dish during subsequent fabrications, so less total mass will be needed. This is unless you need features from both halves of the wafer.
3. Mix the PDMS for 5-6 minutes
4. Pour the PDMS into the petri dish and over the valve master
5. Vacuum for ~1 hour
6. Take the dish out, place the lid on it, and bake in over for 24min at 80C.

PDMS Bonding

1. With both valve and channel wafers baked, take them out and bring into clean room
2. Cut out PDMS blocks from the valve master
3. Each one should be cleaned with scotch tape, on both sides.
4. Place a white wipe on the counter and stick a long, looped, piece of scotch tape on it. All PDMS debris should be stuck to this tape to keep the counter clean
5. Punch holes in the valve layer PDMS blocks using the 0.75mm biopsy punches
6. Use scotch tape to clean the biopsy punch between punches to minimize PDMS debris sticking to the punched holes
7. Can blow the punched holes with the N2 gun as well
8. All PDMS blocks that have been punched should be again cleaned with scotch tape
9. Place a piece of scotch tape on the side of the block that is to be bonded to the channel layer and lay these devices on their back (the side not to be bonded) on a white wipe as you punch additional devices. The counter is generally not clean and the tape will also keep that surface clean as you work.
10. When ready, plasma both the channel wafer and the PDMS block, 30 seconds at 30 Watts.
11. Align carefully and repeat as necessary. Remember to turn off the lid vacuum before lifting the lid. Use tweezers to carefully remove the dummy block with the glass slide so as to not lift and pull on the valve block
12. When all devices have been bonded to the channel wafer, bring it out inside in a petri dish and bake for at least 1 hour at 80C. Can be overnight or 24 hours, doesn't really matter. It's to make sure the two layers fuse. But remember that the longer it's in there, the stiffer the PDMS becomes.

Note: For the alignment, the PDMS block for the valve layer is not thick enough to reach the channel wafer. You will need to cut out an additional dummy block and stick it onto a glass slide. Make sure it's firmly stuck, so it doesn't fall off if held upside down and there are no visible air pockets between the glass and the PDMS. The block to be bonded should be placed on top of this dummy block with tweezers after the plasma treatment. Be careful not to touch the top face of the PDMS block you just plasma treated. Then take the glass slide with the two blocks stacked on it and place it inverted in the space on the aligner lid that is able to hold a glass slide using vacuum suction. Practice positioning the wafer beforehand as well.

Electrode Preparation

1. The glass slides with the electrodes contain more than one set. To cut out individual pieces to make devices, use the diamond scribe and scratch a line where the separation is desired. Do this carefully and as straightly as possible, do not repeatedly scratch. It's not like using a pencil to make a line darker and thicker to see, repeated scratching will make the fracturing a disaster. Try to do it only once if you can.
2. Place the slide on a counter or table, with the piece to be broken off hanging over the side of the countertop or tabletop.

3. Apply even pressure with your thumb on the section to be broken off and hold the slide firmly. It should fracture nicely at the line that was scratched.
4. Clean these with water and ethanol, then blow dry with the N2 gun and cover them in a petri dish to be brought into the clean room.

Final Device Assembly

1. After the PDMS baking is done, bring them into the clean room with electrodes.
2. Cut around each PDMS block with the scalpel and gently peel them off from the wafer
3. Clean the top and bottom sides with scotch tape
4. Again, prepare white wipes and scotch tape to collect PDMS debris and to avoid placing things directly on the counter
5. Punch and clean in the same way as the PDMS bonding protocol
6. Blow the glass pieces with the N2 gun before putting them in the plasma bonder with the PDMS blocks
7. Again, 30 sec at 30 Watts
8. The stage for the aligner should be the small circular and not the big square one that is used for wafers
9. Apply a suction vacuum to the stage and place a dummy block on it. The main PDMS block will be placed on top of this one to give it enough height.
10. The piece of glass with the electrodes will need to be taped to a glass slide. Tape it on the left and right sides, avoiding the electrode metal and not in the region that will be covered by the PDMS block.
11. Invert the glass slide with the electrodes on it and place in the vacuum region of the aligner lid
12. Align carefully and remember to turn off the lid vacuum before raising it. Use tweezers to remove the device from the dummy block
13. When finished, place all devices in a petri dish and bake in oven for at least 1 hour at 80C

Bonding Wires

1. After the assembled device has been baked, cut two pieces of appropriate length wires for each device
2. Do not use the wires that are woven from many smaller threads. Use the one that is a single solid piece
3. Using the wire stripper, remove a section of the rubber sheath from each end, as these sections will be used to make electrical contact
4. You can use regular epoxy glue to hold the two wires in place, attaching them to the glass of the device before applying the silver epoxy
5. Use silver epoxy to connect the wires to the pads of the electrodes. You can use the 10uL pipette tips for this. Be careful not short the electrodes with sloppy silver epoxy work. If it happens, try to scratch off the connection with the scalpel
6. After applying the silver epoxy, each device must be baked in the oven for at least 1 hour at 80C to ensure the silver epoxy cures.

7. You can use a voltmeter to check for conductivity and to ensure there are no shorts afterwards, if you feel the need
8. These wires must be soldered to two points within the aluminum block setup on the microscope stage. After this is done, check that each wire is not shorted with the metal surface surrounding the soldering points using the voltmeter

Lift-off Process

1. Preparing Microscope Slides Can be cleaned using sonicator (look up how you want to do it). Or can be cleaned using piranha (see piranha etch protocol). Prepare at least 5-10 extra slides as losses will happen.

2. Setup Wrap a hot plate with aluminum foil. Program the spin coater:
a. 10s @ 500 RPM, ACL = 015
b. 30s @ 3000 RPM, ACL = 010
c. 20s @ 200 RPM, ACL = 005

Set the mask aligner timer to 15 seconds, and position your mask.
3. 10 min @ 200ºC Place slides on hot plate at 200°C for 10 minutes, then let cool 2 min. This step removes any adsorbed humidity from the surface of the slides.

4. Spin coat Place a slide on the spin coater (slide attachment) and vacuum in place. Use the Pasteur pipette to dispense ~1 mL of S1813 photoresist.

5. Prebake 60s @ 95ºC Place slide on hot plate for 60s at 95ºC.

6. UV Expose 15s Place slide on stage. Close lid, make final positioning adjustments and bring the stage up until you feel resistance, and then slide under the lamp. Do not look at UV lamp, wear eye protection or turn away.

7. Toluene soak 60s + N2 dry Place slide in toluene dish for 1 minute. In this step, the top of the photoresist is being chemically modified to develop slower than resist underneath (top is less soluble). This leads to undercut features favorable to lift-off. Dry with high-purity nitrogen.

8. Postbake 15s @ 95ºC Place slide on hot plate, and bake for 15s. Remove with tweezers, place on aluminum foil for 1 min cooling.

9. Develop in diluted Tetramethylammonium hydroxide (TMAH) + N2 dry Create a solution of diluted TMAH: 6 mL of TMAH in 76 mL of deionized water in the glass dish, and place above a (cool) hot plate. Note that this solution behaves differently for the first slide compared to later slides. The first slide that is immersed will likely be wasted, as the solution is initially aggressive and MUST be removed at 45 seconds. As more and more slides are exposed, the solution slowly loses its potency (development time can reach 2mins eventually). TMAH solution can be replaced after at least 4 slides (be sure to clean to the glass dish before preparing next solution). It is *very* important not to overdevelop (will see cracking of photoresist around features). After development, use the tweezers to transfer a slide to a glass beaker with deionized water. Rinse the slide gently in the water for 1min by moving it in and out. N2 dry **VERY CAREFULY**. Use a gentle stream as it's possible to blow of features.

Note: During development watch for the features to appear on the slide (will be faint red at first). Once it is dark red (time varies, can be 20 sec if fast or 35-40 sec if slow) agitate constantly by hand and watch for features to clear, then remove.

10. Microscope verification Use the microscope to verify slide quality, and adjust procedure as necessary. Place slides into case with photoresist side all facing one way, label the bottom of the case using a piece of tap indicating the direction. Blow the inside of the case with the N2 gun in the clean room beforehand to clean it. Once outside do not open the case.

11. Metal deposition Once 20 slides are complete (1 batch), deposit a 50nm Au layer with 5nm Ti adhesion layer. This can be performed at the Carleton University MicroFabrication Facility. Use e-beam evaporation.

12. Lift-off with N-Methyl-2-pyrrolidone Use NMP to etch the photoresist, leaving only the metal-on-glass electrodes. The etchant should be heated to 70°C to accelerate the process. Use a magnetic stir bar but be careful not to let your slides get under the stir bar. Use a reasonable spin speed as to not have excessive splashing. The crystallization dish can fit 3 slides at once. This process generally takes 30 minutes. Rinse with deionized water after most of the gold has flaked off. Residual gold can be removed using the squirt bottle's jet. Blow dry gently.

Wet-etching with Aqua Regia and Hydrofluoric Acid

1. As I recall they can fit 20 slides per run. So piranha clean this many. Bring all slides into clean room, bake off water at 200°C for 10 minutes, let cool for 2 minutes, and place into case. Mind the top face of the slides. All slides facing up during piranha should remain face up, and this same face should all be aligned in the same direction in the case. Indicate inside the case with tape the side of the slides that is to have metal deposited.

2. Request 50nm Au and 5nm Ti using electron beam evaporation. (or Au-Cr if you understand it's acceptable for your use)

3. When slides come back, bring into clean room. Set spin coater to 500 rpm 10 sec (lowest ACL should be fine), 1000 rpm for 30 sec, and 10 sec to ramp down. For other ACL, use something reasonable. How many slides you process is up to you. I usually do 5 or 6.

4. Use positive photoresist. It should be poured into a smaller bottle and dispensed onto the slide using a glass pipette. Can use S1813 or AZ.

5. Exposure is 60 sec. But adjust as you see fit. Can consider rehydration if using AZ, but not necessary. Develop the photoresist. Look up what to do depending on which resist you use; AZ has same procedure for wafers and we have a stripper for S1813. Rinse with water squirt bottle and dip slide in and out of beaker with DI water for 1 min. Blow dry gently.

6. Bring slides out of clean room. Some photoresist may not be removed. If that's the case, place them under the stereo microscope and scratch off the photoresist with the Exacto knife. The regions you need to scratch off are areas where the covered gold would bridge each pair of electrodes. You must avoid a short.

7. To etch gold, prepare Aqua Regia. The speed and strength is dependent on how much water is used. For me, I use 1:1 acid solution to water. HCl to nitric is 3:1. If using this, I recommend 30mL HCL, 10mL nitric, and 40mL water. Water first obviously. Acids are not from diluted stocks, use max concentration, same as when purchased. Also prepare a separate water bath.

8. Do not leave the solution and go off somewhere else. When prepared, use immediately, it loses potency with time. I find agitation is not necessary and even slows it down. You should notice the gold just vanish. Shouldn't take more than 10-15 seconds. You can

leave it in for an extra 2-3 seconds after seeing the gold vanish to ensure it's all removed. But be aware that horizontal etching does occur. Based on user experience, preparing more aqua regia may be necessary as potency weakens with use (and naturally you may need a bit longer on the later slides than the first). I vaguely recall 4-5 per mixture but use your judgment.

9. Pull it out place it into the water bath. After all slides are done, remove them from the water bath one by one and rinse with DI water bottle, then blow dry. The underlying Ti (or Cr) will appear dark/black if compared to a normal glass slide.

10. The etchants for these metals work by removing the metal oxide layer, regenerating it, and repeating. If adhesion layer is Cr, we have a commercial Cr/CrO etchant. Pour enough to cover a glass slide into a dish and prepare a separate water bath. In our experience, 10-15 seconds with agitation is enough to remove Cr. After, place slide into water bath, dump etchant into acid waste beaker, and pour in some more for next slide. When finished, rinse slides with DI water again, and blow dry. Check that the adhesion layer is removed with voltmeter by touching down in two blank areas on the slide.

11. If adhesion layer is Ti, buy either commercial etchant (which will contain HF) or use the stuff we have bought in the past (which contains some kind of ammonia oxide-based chemical). As stated before, pure HF will not do the job; you need something else that can regenerate the metal oxide layer. So HF is obviously quite dangerous, we have a calcium cream in the common lab. Keep it ready at all times, and wear full protection (like for piranha). If HF is splashed on you, remove coats, gloves, or clothing immediately, apply cream, and call for help.

12. Prepare one dish with HF and one dish with water. Keep sink water running at all times. Rinse gloves thoroughly after handling bottle. Ben made a white dipper, you can place two slides onto it, and then place dipper into the HF bath with slides submerged.

13. Rotate and move slides by moving dipper, for about 30 seconds. Lift dipper up—not out of the dish itself, just above the surface of the HF—and carefully pour out as much solution as possible back into the dish.

14. Dunk dipper into your water bath and bring the whole thing to the sink. Place the dish below the water stream and let it fill to the full volume and overflow for a bit. Then pour out the water and repeat 3-4 times. Make sure the dish, dipper, and your gloves are thoroughly rinsed.

15. Blow dry the slides. Dump the used HF into your waste container, then rinse dish with water 3 times. By rinse I don't mean place it under the faucet and just let it go. Do not let water spill out, swirl the water around, then dump that into your acid waste too. Pour in fresh HF and prepare a fresh water bath in the second dish and repeat for more slides.

16. Now to remove the protective photoresist layer. You can use the acetone squirt bottle, and then follow up with isopropanol. Then blow dry. Make sure to push off all the acetone. Pay attention to milky residues. You may need to repeat and be more careful or replace the solvents if you suspect they are dirty. Make sure solvents do not get on the gloves and then are blown onto the slide. Degradation occurs and if you blow in the direction of the electrodes, it will smear on them.

17. Finally, inspect for physical defects under microscope (not stereo, its magnification is too weak).

Trapping a Cell

1. Turn on all the electronics and the heating system first, this will allow things to warm up while you perform the other tasks.
2. Using only a culture that is in log phase and is also not opaque from a high cell density, fill a cuvette with 0.5 mL of cell suspension and 0.5 mL of media (different dilutions can be used at your discretion).
3. Pipette the solution in the cuvette up and down to mix it, then bring the cuvette to the spectrophotometer to measure the optical density.
4. Record the OD value and dispose of the cuvette in bleach.
5. Light the ethanol flame and grab a 40 mL vial and a 3 mL test tube.
6. Rinse the 3 mL test tube using the DI-water, then bring it back and sterilize the top portions of both the vial and the test tube using the flame. Then place the test tube into the vial. Be careful not to breathe into the vial or to do it in the presence of people moving about, as this will lead to contamination.
7. Pipette 1 mL of the cell suspension into the test tube that is sitting in the vial, then bring the whole thing to the microscope. Cover the mouth of the vial with your hand (gloves) as you are transporting it.
8. Carefully screw on the white cap that the inlet tubing is inserted into. Make sure that you pinch the tubing with your fingers as you put the cap into place. You must ensure that they don't touch anything and go straight into the 3 mL test tube.
9. Up the inlet pressure to 0.05 MPa and wait for a minute to allow the flow of cells to be established.
10. Run the LabVIEW program and click the big button labeled "Adjust". It should now be lit up in bright green. This sets the outlet regulators to the "Low" pressure condition. "Low" uses the pressures set under "Initial L, High" and "Initial R, Low". Note that these numbers are in units of PSI.
11. Once the Adjust button is activated, the pressures can only be modified using the hotkeys on the keyboard and cannot be changed by clicking things in the program unless the Adjust button is clicked again to deactivate the function.
12. Place the keyboard next to the microscope so you can use while looking through the eye piece. A wireless keyboard or a USB extension is needed.
13. Labeled with orange tape on the keyboard are the hotkeys that control the pressures. The Insert key is associated with the left arrow, and pushing it sets the pressure conditions to "Low". Pressing Home increases the flow speed towards the left (left in the view of the miscroscope). Pressing Page Up decreases the speed and can reverse flow direction. The Delete key sets the pressure condition to "High". Pressing End

increases the flow speed going to the right and pressing Page Down decreases the flow speed. Use these keys to help adjust the pressures during trapping.

14. Use the manual regulator to slow down the flow until you can actually see cells flowing from the inlet into the bypass. You will need to use a combination of the manual and computer controlled regulators to slow down the cells and to ensure that one will flow into the sensing channel in the direction you want it to.
15. Once a cell begins moving into the channel, you must be quick to crank up the pressure on the regulator controlling the valves in order to trap the cell. Go to at least 0.2 MPa.
16. At this point, you can change the media, take an image, or do whatever.
17. When that is done, partially lift the valves. This value may vary based on PDMS stiffness. My recommendation is to set the inlet pressure to 0.035 MPa. At this pressure, 3 mL of solution can last roughly 8 hours before running out.
18. After setting the inlet pressure, use the keyboard hotkeys to shuffle the cell back and forth and adjust the speed so that it's not too fast and not too slow either. A good starting speed will really help the program out.
19. When ready to begin the automation, make sure to deactivate the "Adjust" function by clicking the button so it turns off. Then stop the LabVIEW program (don't close it) by hitting the little red stop sign near the top of the GUI. This will reset the time and create a new .dat file.
20. Start the program again. Click the Peak Analysis and Detection Active buttons so they're on. Then manually click the white "P Condition" box under "Ramp" and change it to the opposite pressure condition that you left it at (change to High it was on Low and change to Low if it was on High). This will reverse the flow so that the cell will flow past the electrodes and trigger the first measurement.
21. The program should now automatically begin data taking and flow reversing. You should now click the little button that is bottom-right of "Rev Kick". This is will tell the program to that it should automatically change the pressure condition if it does not record an event for a certain period of time. This duration is set in the "Threshold(s)" box. I recommend 8 seconds. This function helps to deal with the events that fail to register.
22. The "Target Width(ms)" and "Tolerance" can also be set. This tells the program to aim for a certain transit time. Pressures will not be adjusted if the transit time is within the range set by the tolerance (plus or minus some amount around the target time).
23. When ending an experiment, make sure to click the two red rectangular "STOP" buttons in the bottom-left of the GUI. This will stop the data taking and pressure control loops and output the current drop % data in a CSV file in the folder you specified.
24. After the experiment, flush with 2 mL of DI-water, and remember to rinse the test tube and sterilize both the test tube and the large 40 mL vial using the flame. Make sure you don't deplete all the water as you should avoid getting air into the channels.